Evaluation of Multiple Planetary Boundary Layer Parameterization Schemes in Southeast U.S. Cold Season Severe Thunderstorm Environments

ARIEL E. COHEN[a]

School of Meteorology, University of Oklahoma, and NOAA/NWS/NCEP/Storm Prediction Center, Norman, Oklahoma

STEVEN M. CAVALLO

School of Meteorology, University of Oklahoma, Norman, Oklahoma

MICHAEL C. CONIGLIO AND HAROLD E. BROOKS

NOAA/National Severe Storms Laboratory, Norman, Oklahoma

ISRAEL L. JIRAK

NOAA/NWS/NCEP/Storm Prediction Center, Norman, Oklahoma

(Manuscript received 9 November 2016, in final form 20 July 2017)

ABSTRACT

Southeast U.S. cold season severe weather events can be difficult to predict because of the marginality of the supporting thermodynamic instability in this regime. The sensitivity of this environment to prognoses of instability encourages additional research on ways in which mesoscale models represent turbulent processes within the lower atmosphere that directly influence thermodynamic profiles and forecasts of instability. This work summarizes characteristics of the southeast U.S. cold season severe weather environment and planetary boundary layer (PBL) parameterization schemes used in mesoscale modeling and proceeds with a focused investigation of the performance of nine different representations of the PBL in this environment by comparing simulated thermodynamic and kinematic profiles to observationally influenced ones. It is demonstrated that simultaneous representation of both nonlocal and local mixing in the Asymmetric Convective Model, version 2 (ACM2), scheme has the lowest overall errors for the southeast U.S. cold season tornado regime. For storm-relative helicity, strictly nonlocal schemes provide the largest overall differences from observationally influenced datasets (underforecast). Meanwhile, strictly local schemes yield the most extreme differences from these observationally influenced datasets (underforecast) in a mean sense for the low-level lapse rate and depth of the PBL, on average. A hybrid local–nonlocal scheme is found to mitigate these mean difference extremes. These findings are traced to a tendency for local schemes to incompletely mix the PBL while nonlocal schemes overmix the PBL, whereas the hybrid schemes represent more intermediate mixing in a regime where vertical shear enhances mixing and limited instability suppresses mixing.

1. Introduction

Accurately representing turbulent processes occurring within the planetary boundary layer (PBL) of the lower troposphere is of particular importance for the southeast U.S. cold season severe thunderstorm environment (Cohen et al. 2015, hereafter CCCB15). In southeast U.S. cold season severe thunderstorm environments (hereafter SECOLD), thermodynamic instability is often limited amid ample vertical wind shear, and the marginality of thermodynamic instability for the SECOLD regime is found to be a distinguishing characteristic of this environment compared to other severe thunderstorm environments (e.g., CCCB15). Small forecast inaccuracies in such scenarios involving the marginality of a parameter supporting high-impact weather may be of particular importance, and a source of these inaccuracies comes from a model's representation of the low-level wind profile and the low-level thermodynamic profile (e.g., Jankov et al. 2005;

[a] Current affiliation: National Weather Service, Topeka, Kansas.

Corresponding author: Ariel Cohen, ariel.cohen@noaa.gov

DOI: 10.1175/WAF-D-16-0193.1

Stensrud 2007; Hacker 2010; Hu et al. 2010; Nielsen-Gammon et al. 2010). Ultimately, this motivates the need to minimize errors in forecasting the vertical atmospheric structure (the boundary layer in particular) to better depict characteristics of the convective environment and subsequently increase the ability to more accurately assess a severe weather threat (e.g., Kain et al. 2003, 2005, 2013).

Turbulent eddies facilitate the exchanges of momentum, heat, and moisture in the PBL within which properties of surface conditions are communicated on time scales under an hour (e.g., Stull 1988; Stensrud 2007). Because these eddies cannot be explicitly resolved by mesoscale (grid lengths typically at least 4 km) models that have been in use operationally for many years, their effects are represented using PBL parameterization schemes. The theoretical development of these schemes is addressed by multiple sources (e.g., Stull 1988; Holton 2004; Stensrud 2007). The Advanced Research version of the Weather Research and Forecasting Model (WRF-ARW; Skamarock et al. 2008) offers options of different PBL parameterization schemes to choose from when configuring numerical simulations of weather events. However, some schemes may be more appropriate for use in certain atmospheric regimes than others (e.g., SECOLD versus other regimes). The appropriateness of using particular schemes is dependent upon the vertical thermodynamic structure and related instability, which is addressed in further detail within a summary table for different PBL parameterization schemes as provided by CCCB15.

CCCB15 summarize basic foundational work in the development of PBL parameterization schemes by synthesizing explanations provided by Stensrud (2007) and Stull (1988). One-way PBL parameterization schemes are distinguished by the depth through which known variables are permitted to affect a given model point (''local'' or ''nonlocal''). For local closure schemes, only vertical levels that are immediately adjacent to a given point within the model directly influence variables representing this point, whereas this restriction is relaxed in nonlocal closure schemes. Thus, nonlocal closure schemes are able to represent the effects of deeper PBL circulations and can improve model accuracy for regimes in which larger eddies are a substantial source of vertical transport in the lower atmosphere.

Stensrud (2007) highlights a major disadvantage of employing strictly local closure, which effectively reflects stunted deepening of the PBL in the presence of localized stable layers. Stable layers inhibit vertical mixing within the PBL, which is facilitated by the largest eddies encouraging deeper mixing of mass, heat, and momentum. Nonlocal schemes are able to account for the effects from these eddies. Some schemes have been developed that incorporate concepts of both local and nonlocal closure, which will be the focus of later discussion, with an emphasis on the Asymmetric Convective Model (ACM), whose design is illustrated by Pleim (2007a,b).

CCCB15 provide an in-depth collection of typical biases associated with PBL schemes used in the WRF that have been explored throughout the broader literature. A tabular summary of these PBL schemes and others, along with associated advantages and disadvantages based on a variety of sources, is provided by CCCB15. However, prior to CCCB15, meteorological regimes for which previous studies have addressed the evaluation of PBL schemes have not included a sole focus on the southeast U.S. cold season severe weather patterns. Vertical motion at larger spatial scales, shear-driven eddies, as well as daytime surface heating can all influence thermodynamic and kinematic structures in the low levels of the atmosphere. King et al. (2017) establish the importance of warm-air advection in distinguishing low-CAPE environments supporting severe events. CCCB15 highlight examples of observed and model forecast soundings in SECOLD environments that are neither well mixed nor strongly stable, yet such PBLs need to be accurately portrayed by model simulations using PBL parameterization schemes to resolve the highly sensitive instability parameter space characteristics of the regime.

The performance of PBL schemes may substantially influence the ability of a numerical model to accurately simulate the southeast U.S. cold season severe weather environment (CCCB15). CCCB15 investigate two SECOLD-regime severe weather events, which highlight differences in the thermodynamic and kinematic structures between this regime and those of a more quiescently evolving PBL. They illustrate the SECOLD tornado environment using an observed sounding to show its characteristic low static stability in the low levels with strong vertical wind shear. However, no portion of the observed sounding exhibits well-mixed layers characterized by uniform potential temperature and/or wind velocity. As such, in a general sense, this environment represents the thermodynamic and kinematic vertical profiles characteristic of neither well-defined strong-mixing nor strong-stability regimes, highlighting its complexity as an intermediate hybrid regime for which research preceding CCCB15 has been limited.

CCCB15 find that nonlocal mixing is necessary to properly simulate the relatively steeper low-level lapse rates within the warm sectors of an extratropical cyclone favoring the severe weather for the two cases examined therein, as local schemes yield lapse rates that are too weak. The importance of properly simulating 0–3-km

lapse rates is critical in these environments owing to their ability to discriminate between significantly severe and nonsevere thunderstorm environments (Sherburn and Parker 2014). CCCB15 find nonlocal schemes to depict weaker storm-relative helicity (SRH) compared to local schemes in association with a somewhat smoother vertical wind profile, but the SRH is still sufficiently strong to suggest that the deeper mixing inherent to the nonlocal schemes does not produce too smooth of a wind profile to preclude tornadoes. The conclusions of CCCB15 provide the motivation for the present study, to extend the analysis to a larger, more diverse sample. As such, this work extends the investigation of PBL schemes in the SECOLD regime by incorporating many additional cases in order to better generalize results while better substantiating an understanding of the tendencies of the PBL schemes through an investigation of multiple convective parameters. Furthermore, this study decomposes these tendencies into diurnal and nocturnal components since significant nocturnal tornadoes are not uncommon in the southeast United States (e.g., Kis and Straka 2010), especially when considering linear convective modes (Trapp et al. 2005). Ultimately, this will allow for an assessment of the performance of the PBL schemes, which can provide a basis for determining which schemes best depict the SECOLD regime and can also provide an opportunity to improve upon the parameterization schemes for this regime.

Subsequent discussion and analysis focus on a sampling of five PBL schemes: two local, two nonlocal, and one hybrid local–nonlocal and four variants of the hybrid. The two local schemes considered are the Mellor–Yamada–Janjić (MYJ; Janjić 1990, 1994) and quasi-normal scale elimination (QNSE; Sukoriansky et al. 2005) schemes, the two nonlocal schemes considered are the Medium-Range Forecast (MRF) model (Hong and Pan 1996) and Yonsei University (YSU; Hong et al. 2006) schemes, and the hybrid local–nonlocal scheme for which variants are created herein is version 2 of the Asymmetric Convective Model (ACM2; Pleim 2007a). This set of five PBL schemes and variants is intended to reflect the physical dispersion of model simulations arising from the two principally different techniques of representing vertical mixing using PBL parameterization schemes: local versus nonlocal mixing.

Following a review of the distinguishing characteristics of the SECOLD environment in section 2, the present study broadens the scope of CCCB15 to a more diverse dataset of 21 different severe weather events as opposed to 2 in CCCB15. The experimental design and many aspects of the evaluation process are identical between the present work and CCCB15 in order to retain consistency and so the details are only partially reiterated in section 3. The mathematical background for testing the sensitivity of the ACM2 scheme is offered in section 4. Statistical analyses representing the full 21-event SECOLD simulated dataset are provided in section 5 for several thermodynamic and kinematic variables. This includes investigation of diurnal versus nocturnal statistical tendencies among the full dataset. Section 6 provides a discussion of the differences in simulated convective morphology owing to variations in the PBL scheme.

2. Characteristics of the SECOLD environment

Severe thunderstorms (producing hail $\geq$ 1-in. diameter; wind gusts $\geq 50\,\text{kt}$, where $1\,\text{kt} = 0.51\,\text{m}\,\text{s}^{-1}$; or a tornado) are responsible for a wide array of impacts to society. The meteorological conditions that favor these phenomena (e.g., Schaefer 1986) must simultaneously be met in time and space, and include instability, moisture, and lift. An additional condition of vertical wind shear is required for organized severe thunderstorms to occur. This work focuses on the specific environment of tornadic thunderstorms that occur in the southeast United States during the cold season (i.e., December–February), and is specifically intended to highlight some of the distinguishing characteristics of the SECOLD environment. The societal impact of such events is particularly substantial owing to socioeconomic characteristics of the Southeast that inherently make this area more vulnerable to severe weather casualties (Ashley 2007).

Previous studies have investigated the characteristics of the southeast U.S. tornado environment (e.g., Guyer et al. 2006; Guyer and Dean 2010). Sherburn and Parker (2014) consider high-shear, low-CAPE (HSLC) environments in general (not limited to the southeast United States in the cold season) and evaluate the performance of a broad set of meteorological parameters in these environments for the prediction of severe thunderstorms. Also, southeast U.S. cold season severe weather environments and European severe storm environments tend to have similar characteristics (Brooks 2009).

For the purposes of building upon the previous work and highlighting distinguishing characteristics of the SECOLD environment—particularly relevant for motivating further work related to better understanding the PBL of this environment—this study subsequently provides a parameter-based analysis of a subset of often-referenced meteorological variables for the southeast U.S. cold season tornado environment. To accomplish this, we use the dataset presented by Smith et al. (2012), Thompson et al. (2012), and Edwards et al. (2012) (collectively referred to as STE12 hereafter).

STE12 introduce, document, and apply the process of merging severe storm reports with near-storm environmental characteristics based on the Storm Prediction Center (SPC) mesoanalysis data. Also, STE12 document the assignment of environmental characteristics and modes associated with certain severe weather–producing convection across the United States, serving as the foundation for this work. The resulting dataset is a 9-yr sample of tornado, significant hail (hail of at least 2 in. in diameter), and significant wind (wind gusts of at least 65 kt) events based on the National Centers for Environmental Information *Storm Data* publication that is paired with SPC mesoanalysis data (Bothwell et al. 2002) during the period from 2003 through 2011. This involves the documentation of the highest-magnitude report per hour and per report type on the 40-km grid-length Rapid Update Cycle (RUC) model grid (Benjamin et al. 2004), permitting pairing of the severe report database with the mesoanalysis data. This process amounts to the collection of 22 901 total severe thunderstorm grid-hour events, with 10 753 of them corresponding to tornadoes, which are the subject of subsequent focus.

The 10 753 grid-hour tornado events are stratified into two groups: 1) tornado events occurring within roughly the southeast quarter of the United States and during the cold season (December–February), referred to as SECOLD (503 events), and 2) tornado events occurring outside of the SECOLD spatiotemporal environment, referred to as NONSECOLD (10 250 events). We define the southeast United States to encompass the states of Arkansas, Louisiana, Tennessee, Mississippi, Alabama, Georgia, North Carolina, South Carolina, and Florida. NONSECOLD includes events outside of the southeast United States any time of year and within the Southeast outside of the December–February period. The motivation for the aforementioned stratification process is to investigate the difference between meteorological variables associated with SECOLD tornadoes and those associated with other tornadoes occurring across the country and during warmer times of year.

Box-and-whisker plots for selected thermodynamic and kinematic variables characterizing the SECOLD and NONSECOLD environments are provided to illustrate thee general differences between their corresponding distributions. Displayed plots of the NONSECOLD environments represent a subset of the full distribution of these environments, owing to the substantial disparity in sample size between the smaller SECOLD and larger NONSECOLD distributions. Specifically, random sampling without replacement from the full NONSECOLD distribution is performed for each variable, to create a NONSECOLD sample whose size is equivalent to that of SECOLD. This permits the comparisons between these two distributions to be founded upon more similar quantities of data. Although not shown, it was found that the process of random sampling from the larger sample resulted in little difference in the box-and-whisker plots for all variables subsequently illustrated, precluding the performance of this procedure more than once for any given variable.

Box-and-whisker plots of surface-based (SB) convective available potential energy (CAPE) (SBCAPE) and mixed-layer CAPE (MLCAPE) (Fig. 1) show the downward-shifted, compressed nature of CAPE for the SECOLD environment in comparison to other environments (NONSECOLD). This difference is influenced by warmer and moister conditions (not shown; based on potential temperature and mixing ratio) in the lower atmosphere and steeper temperature lapse rates in the middle atmosphere during the warm season that can support greater CAPE for the NONSECOLD distribution. A consequence of this smaller range of CAPE values is that small increments of CAPE in the SECOLD environment (e.g., those related to forecast and/or observation error) are a larger fraction of the total CAPE compared to that of other environments.

The differences in the portion of MLCAPE confined to the lowest 3 km of the atmosphere between SECOLD and NONSECOLD are smaller than the differences in MLCAPE derived from the entire vertical profile (cf. Figs. 1 and 2). This is associated with larger proportions of MLCAPE confined to the lowest 3 km above ground during SECOLD compared to NONSECOLD (Fig. 2) and highlights the relative importance of lower-atmospheric thermodynamic structures in explaining the CAPE in the SECOLD environment (CCCB15). Furthermore, there is substantial separation between the SECOLD and NONSECOLD distributions of 0–1-km SRH and 0–1-km vertical bulk shear (Fig. 3). Given that vertical thermodynamic and kinematic profiles, whose characteristics are described by these parameters, are directly influenced by turbulent exchanges in the PBL, this provides substantial motivation for further exploration of the PBL in more detail for the SECOLD environment.

3. Methodology

a. Experimental design

The overall simulation design and model evaluation technique follow those presented by CCCB15, with equivalent comparisons in the extension to a much larger sample for the present work. Model simulations are run using version 3.3.1 of the WRF-ARW Model (Skamarock et al. 2008). While this is an older version of the WRF, and subsequent WRF versions could provide

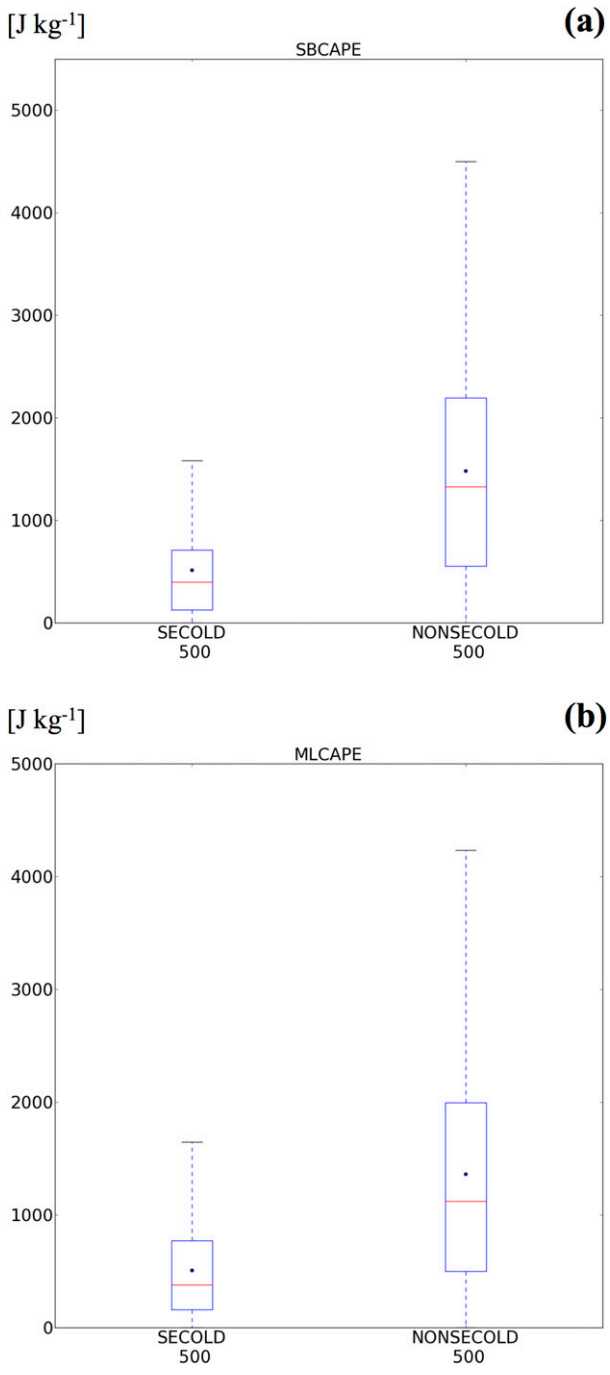

FIG. 1. Box-and-whisker plots corresponding to the distribution of (a) SBCAPE and (b) MLCAPE for tornadoes occurring in the SECOLD and NONSECOLD environments from left to right in each panel with sample sizes listed below the *x*-axis labels. The blue outlined box corresponds to the IQR, the red horizontal line corresponds to the median value, the dot marker corresponds to the mean value, and whiskers extend up to 1.5 times the IQR beyond the first and third quartiles. Outlier values are not included to ensure primary focus on the details of the bulk of the distributions. Distributions corresponding to NONSECOLD environments represent a subset of the full NONSECOLD sample following the procedure of sampling without replacement as described within the discussion.

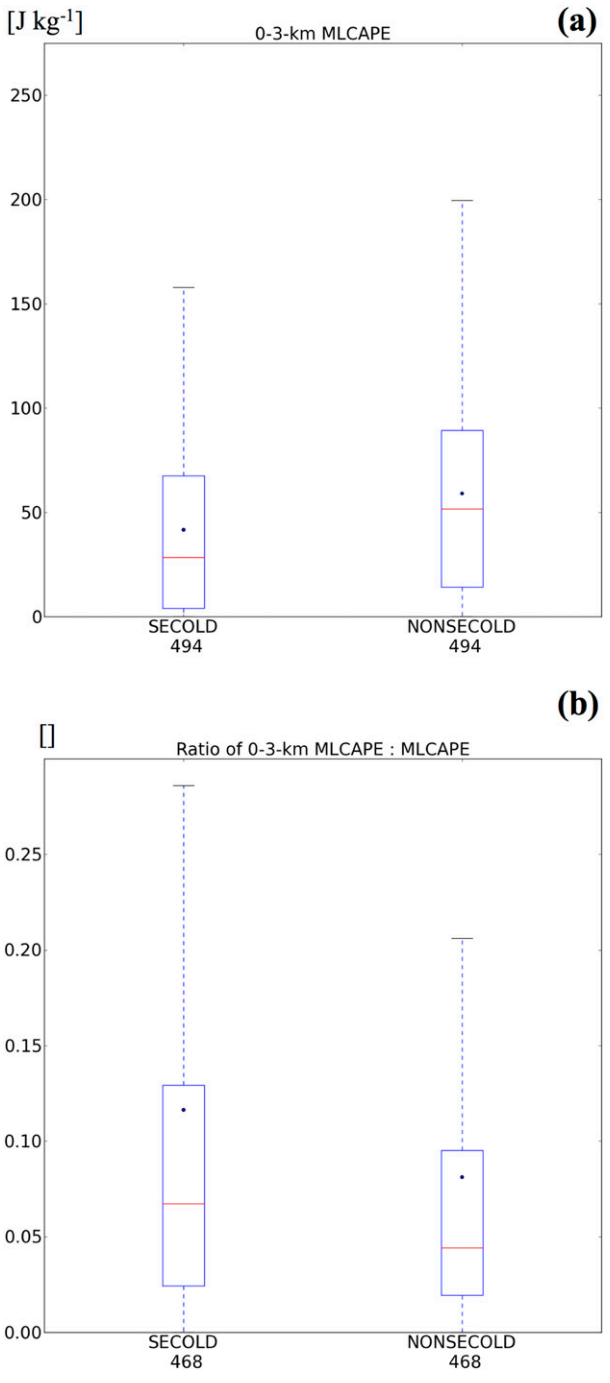

FIG. 2. As in Fig. 1, but for (a) 0–3-km MLCAPE and (b) ratio of 0–3-km MLCAPE to total MLCAPE. Note that the ratio of MLCAPE values corresponds to a dimensionless quantity, as reflected by the *y*-axis label of [].

different results, the basic core structure of the WRF and the behavioral characteristics and differences among the parameterization schemes are expected to be replicated owing to consistencies inherent in the design of this model and its associated schemes. Updates to

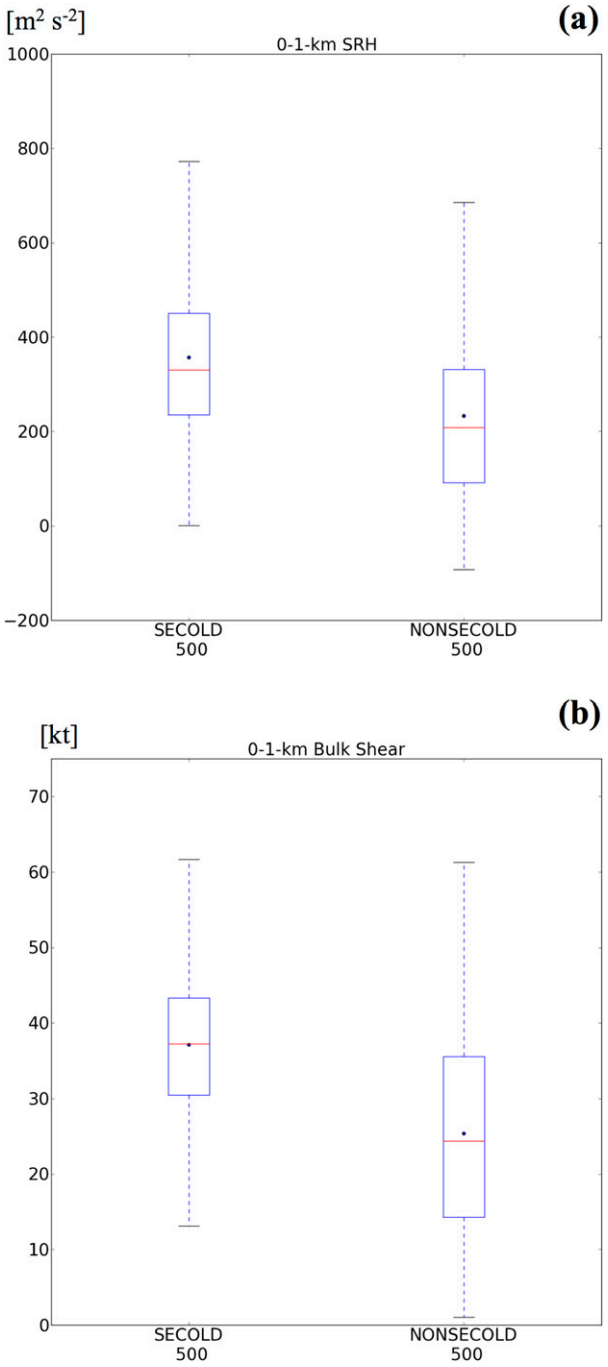

FIG. 3. As in Fig. 1, but for (a) 0–1-km SRH and (b) 0–1-km bulk shear.

WRF occur too frequently for statistical postprocessing in the present study to be complete before subsequent, newer versions of the WRF are available. Ultimately, substantial time has passed between the release of WRF-ARW version 3.3.1, and it would be ideal to use a more recently updated version of the WRF; however, the purpose of the present work is to ascertain a general understanding of the behaviors of the different PBL schemes that can be employed within the WRF framework, and this is accomplished in an established version of the WRF.

The present study uses horizontal grid spacing of 4 km and 50 vertical levels. Grid-point dimensions are 580 grid points in the west–east direction with 350 grid points in the north–south direction. Vertical grid spacing stretches with height above the ground, with around 20-m spacing between levels near the ground stretching to 500-m spacing between levels near the troposphere, with around 8–12 levels typically in an afternoon, relatively well-mixed boundary layer. The domain covers the southeastern United States and vicinity including portions of the Gulf of Mexico, which is illustrated in Fig. 4. CCCB15 specify other characteristics of these WRF simulations, including consistent pairing of the PBL schemes to land surface schemes, initial and boundary conditions using the National Centers for Environmental Prediction Final (FNL) Operational Global Analysis (NOAA/NCEP 2000), the single-moment 6-class microphysics scheme (Hong and Lim 2006), the Rapid Radiative Transfer Model relevant for general circulation models (RRTMG; Iacono et al. 2008) longwave and shortwave radiation schemes, the Noah land surface model (Ek et al. 2003), a model time step of 12 s, and a radiation time step of 30 min. It is acknowledged that this radiation time step is relatively long, which could influence the simulated PBL development. However, given the large quantity of cases simulated for the present study, this radiation time step was chosen to carry out the numerical simulations in a timely manner while also supporting depictions of PBL growth sufficiently consistent with that of the real atmosphere.

Nineteen events are simulated, each involving separate 24-h periods starting at 1200 UTC during which severe weather, including tornadoes, occurred over the southeast United States. In addition to the two cases from CCCB15, this results in a total of 21 separate severe weather events, providing a much larger sample size in the resulting model analyses and across many SECOLD regime episodes. These events were chosen based on a subjective assessment of their production of high-density severe weather reports and the issuance of supporting watches and warnings from the National Weather Service. Figures 5–7 illustrate the superposition of storm reports from these 21 events, along with markers of the four locations considered for forecast sounding evaluation in each event. The decision to select four locations is somewhat arbitrary, but is intended to provide a sample of some spatial diversity of the environment for each event, and is consistent with the analysis procedure carried out by CCCB15. The four particular

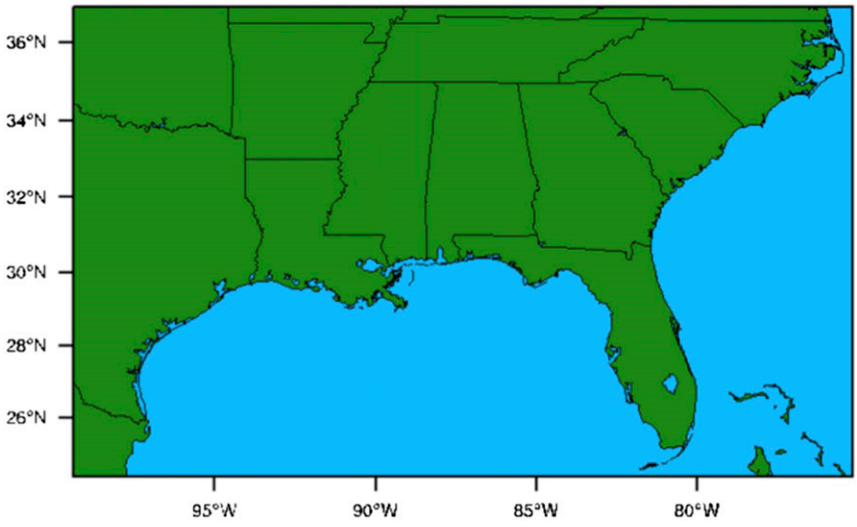

FIG. 4. The domain used for WRF simulations. The horizontal grid spacing is 4 km for the simulations.

locations for each event are based on their proximity to severe thunderstorm reports, particularly tornadoes.

b. *Evaluation process*

As in CCCB15, this study merges model analysis output from the Rapid Update Cycle (RUC; Benjamin et al. 2004) with objective analyses of surface observations to create a consistent observationally influenced dataset to compare with the model simulations. This is done similarly to the process invoked for the generation of SPC mesoanalysis data (Bothwell et al. 2002), such that the surface-observation-influenced data lie at the base of the vertical profiles. Specifically, vertical profiles of relative humidity, temperature, and wind are extracted from RUC output available from the NOAA National Model Archive and Distribution System (NOAA/NCDC 2014a,b) with 20-km horizontal grid spacing at 25-hPa intervals in the vertical each hour; this is repeated for each hour of each 24-h-long simulation. Such routines are performed for pressure levels above that corresponding to the surface based on the surface objective analysis (SFCOA) output (Bothwell et al. 2002). Then, corresponding surface variables each hour originating from the SFCOA output serve as the base of each profile. The corresponding dataset will subsequently be referred to as the RUC/SFCOA dataset. RUC/SFCOA soundings are generated for each of the locations and during the events illustrated in Figs. 5–7, in order to provide thermodynamic and kinematic profiles reflecting the influences of observations for comparing against the WRF Model simulations.

To identify environments that are representative of the warm-sector air that is relevant for supporting convection with at least some streamwise vorticity, sounding-based parameter thresholds are set for comparisons between forecast soundings and RUC/SFCOA soundings. Thresholds of 25 J kg^{-1} and 25 m^2 s^{-2} of most unstable CAPE and 0–3-km SRH are used, respectively (i.e., representing the overlap of at least very limited buoyancy and SRH minimally supporting convection with streamwise vorticity), for a sounding to be considered for comparison. These thresholds slightly differ from the more general, positively buoyant and convectively uncontaminated characteristics that were presented by CCCB15. This is to further reinforce consistent, reproducible constraints for which sounding comparisons are made that incorporate thermodynamic and kinematic characteristics of warm sector air minimally supporting convection with streamwise vorticity for a much larger sample size. Also, to permit model spinup, all initial-hour soundings (1200 UTC) are omitted from the analysis to account for model simulations to adjust from initial conditions. At a given hour, both forecast and RUC/SFCOA soundings must meet these requirements to be considered for comparison. For each case and for each PBL parameterization scheme, all valid forecast soundings and corresponding RUC/SFCOA soundings and related parameters are compiled for statistical analysis, which we present in section 5.

In terms of describing the real atmosphere, the use of the RUC/SFCOA dataset is limited by bias inherent in the RUC model and by errors in the surface objective analyses. Furthermore, the usage of the local scheme from Burk and Thompson (1989) for parameterizing the PBL in the RUC could also potentially bias subsequent

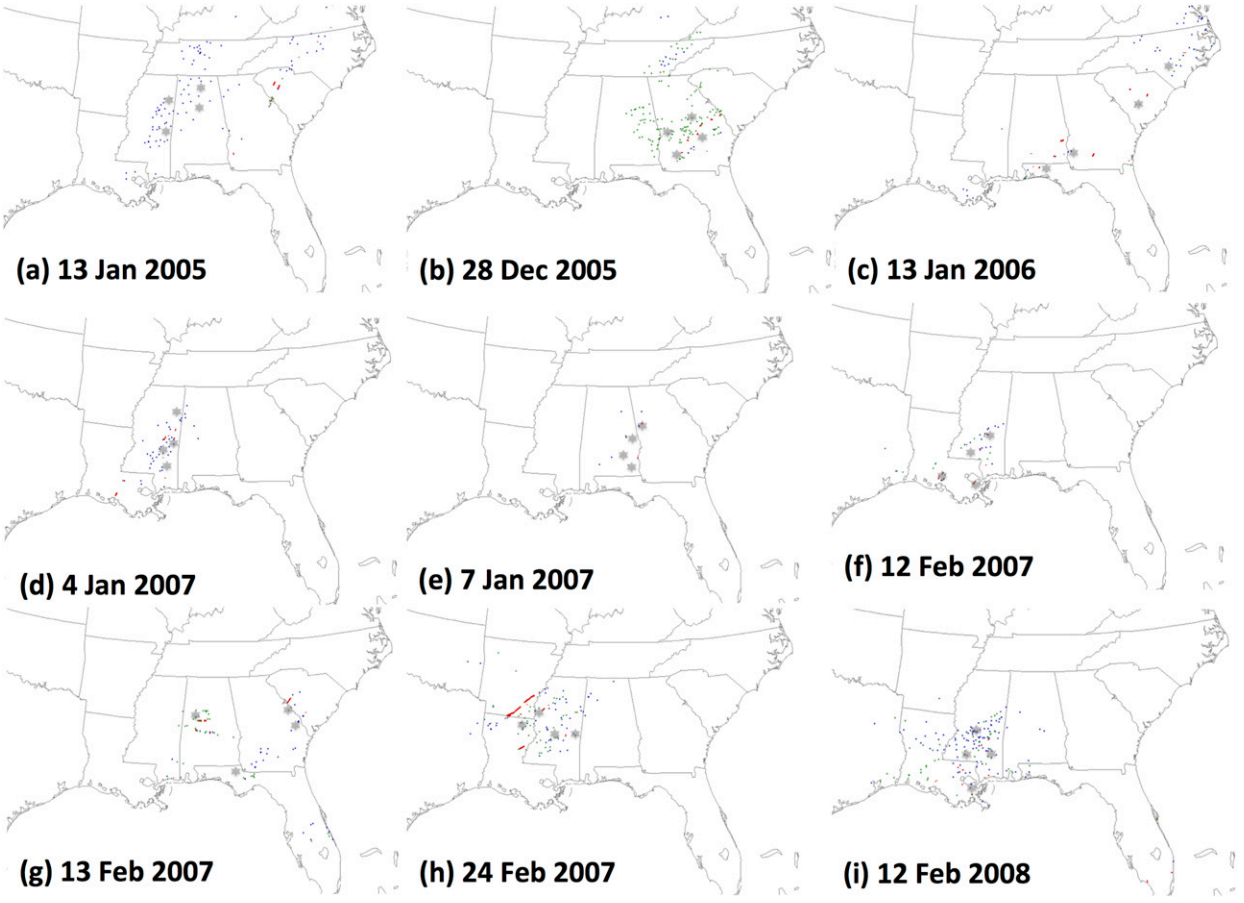

FIG. 5. Severe thunderstorm reports (tornadoes in red, wind in blue, and hail in green) for 9 of the 21 studied events using Storm Prediction Center (2015) overlaid with gray-shaded star markers denoting the four locations used for forecast sounding evaluation for this event. Each event period corresponds to severe thunderstorm reports occurring from 1200 UTC on the listed date in the bottom-left-hand corner of each map until 1200 UTC on the subsequent date. Events are provided in chronological order from left to right and then downward in each row of maps.

results, perhaps in favor of local PBL schemes. RUC/SFCOA is *not* intended to be treated as a purely observational dataset, though it is observationally influenced. The surface objective analysis fields are found to be accurate in severe weather regimes affecting the central United States (Coniglio 2012), and some attempt has been made to evaluate the accuracy of this dataset in the SECOLD regime in section 5. However, despite potential inadequacies, the scarcity of observational data that fully resolve the atmosphere, and irregular spatial sampling of surface observations, prevent a more accurate dataset from being available. Regardless, the operational meteorology community treats the SFCOA system as the standard for real-time, mesoscale analysis, providing backing for its use as a comparison dataset in the present study. While the FNL output, and not the RUC output, was used to initialize the WRF simulations, we believe that this is acceptable as it reflects the various choices of initialization (including non-RUC) options in real-time simulations for which comparisons to the observationally influenced mesoanalysis program can be made. The dispersive sample of forecast soundings evaluated for each PBL scheme across 21 simulated SECOLD severe weather events lends confidence in the building of robust statistical analyses based upon comparisons to the observationally influenced RUC/SFCOA dataset, which, for many, is the modern-era meteorologist's source of real-time mesoanalysis data.

4. Testing the sensitivity of the ACM2 scheme

The notion that the SECOLD regime exhibits intermediate boundary layer mixing (neither highly statically stable nor statically unstable but still yielding CAPE) lends interest in investigating the performance of the ACM2 scheme that combines aspects of both nonlocal and local mixing processes. The nonlocal mixing component and related depictions of a deeper

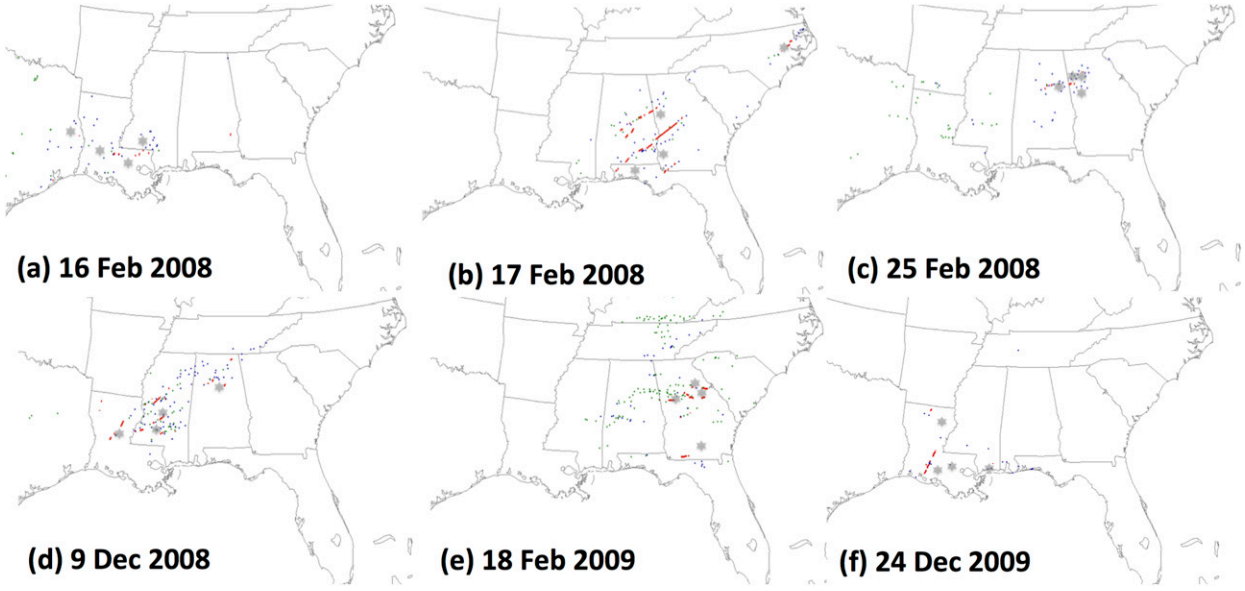

FIG. 6. As in Fig. 5, but for an additional six cases.

PBL would represent the effects of vertical-shear-induced mixing in these environments, whereas the local mixing component may effectively represent the relatively weaker buoyancy-induced mixing in intermediate thermodynamic stability environments. The simultaneous incorporation of 1) enhanced vertical mixing characteristic of strictly nonlocal schemes and 2) suppressed vertical mixing characteristic of strictly local schemes is hypothesized to optimize the performance of the hybrid ACM2 scheme in the SECOLD regime, which also reflects the simultaneous incorporation of enhanced and suppressed mixing (related to strong vertical shear and weak instability, respectively).

The PBL depth simulated by the ACM2 (nonlocal–local) scheme h depends on the critical Richardson number $\mathrm{Ri}_{\mathrm{crit}}$. Specifically, h is determined to be the level at which the bulk Richardson number characteristic of the environmental thermodynamic and kinematic profile defined in Pleim (2007a) Ri_b, becomes equal to $\mathrm{Ri}_{\mathrm{crit}}$ in the entrainment zone. The following is the equation that Pleim (2007a) used for calculating the Richardson number within the entrainment layer

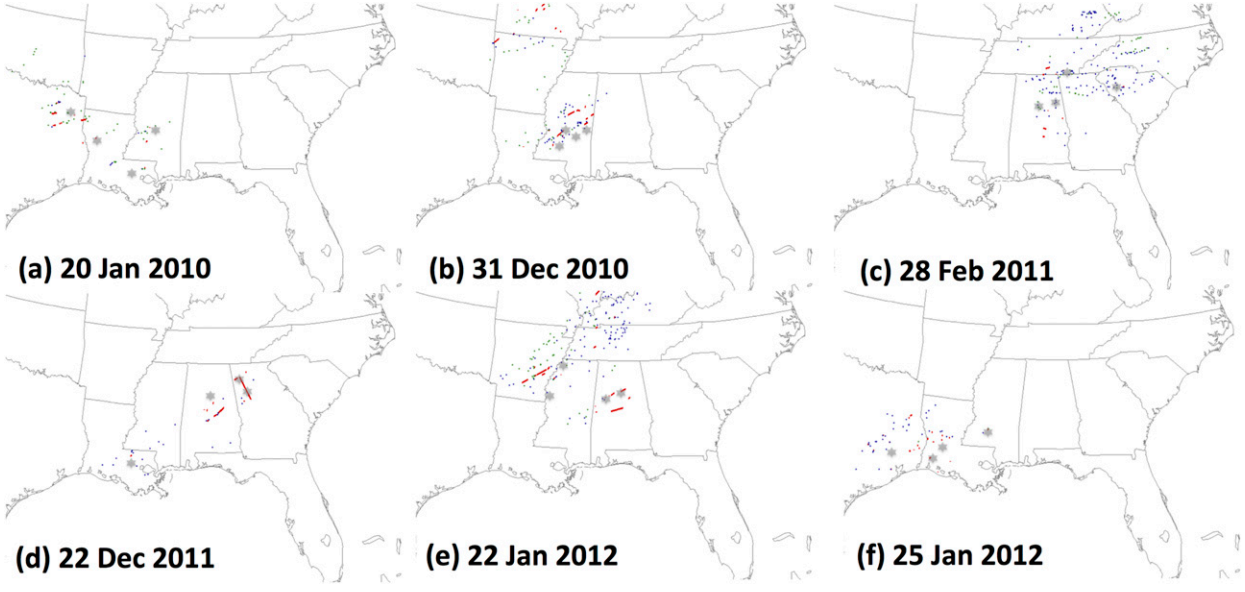

FIG. 7. As in Fig. 5, but for an additional six cases.

that surmounts the mixed layer whose top is defined by z_{mix} corresponding to the top of the convectively unstable layer:

$$\mathrm{Ri}_b = \frac{g[\theta_v(h) - \theta_s](h - z_{mix})}{\overline{\theta_v}[U(h) - U(z_{mix})]^2}, \quad (1)$$

where h represents the height above ground of the top of the PBL, $\overline{\theta_v}$ is the mean virtual potential temperature from the lowest model level to the top of the PBL, θ_s is the virtual potential temperature augmented to account for convective thermals in the lower boundary layer (Holtslag et al. 1990), and the squared difference between $U(h)$ and $U(z_{mix})$ represents the bulk shear within the entrainment zone beneath the PBL height. In addition, g is the vertical acceleration owing to gravity.

The ratio of static stability [vertical virtual potential temperature difference in the numerator of Eq. (1)] to the vertical wind shear [vertical difference in wind speed in the denominator of Eq. (1)] is represented by Ri_b. In general, a larger Richardson number corresponds to greater suppression of turbulence. In turn, the PBL depth then provides definition for the portion of the atmosphere that is influenced by turbulent mixing in these model simulations. Note that the difference between h and z_{mix} physically represents the layer bounded by the top of the mixed layer and the top the diagnostically defined PBL (Pleim 2007a).

Theoretical vertical profiles of virtual potential temperature θ_v and wind components are used to craft Richardson number profiles to better understand implications of the ACM2 sensitivity tests. The default ACM2 (nonlocal–local) scheme uses 0.25 for Ri_{crit}, and four variants to the ACM2 (nonlocal–local) scheme defined by changes to Ri_{crit} are introduced: 0.05 corresponding to ACM05, 0.15 to ACM15, 0.35 to ACM35, and 0.45 to ACM45, with each variant representing the nonlocal–local hybrid configuration. These four values of Ri_{crit} lie within the bounds of the critical Richardson numbers used for the YSU and MRF schemes, 0 and 0.5, respectively, which largely represent a characteristic range of nonlocal-scheme critical-Richardson-number selections in the PBL-scheme literature (e.g., Hong et al. 2006).

To further justify this range of Ri_{crit}, consider a well-mixed boundary layer where $d\theta_v/dz = 0$ from the surface to 350 m beneath exponentially varying θ_v (Fig. 8a) and two profiles of linearly increasing horizontal wind speed in a unidirectional wind profile (Fig. 8b). Two Richardson number profiles in the entrainment zone (between z_{mix} and h) are determined from these profiles, each corresponding to a different strength of vertical shear for the given profile of θ_v (Fig. 8c). The shape of the θ_v profile bears similarity to those of Stensrud (2007) and Stull (1988), where it is assumed for the sake of simplicity that θ_v within the mixed layer is equal to θ_s. In Eq. (1), $\overline{\theta_v}$ is computed as the average θ_v for the entire atmosphere beneath h. This simple model allows us to understand the relationship between vertical wind shear and Ri_{crit} within the entrainment zone above the mixed layer. The equations used to create the profiles shown in Fig. 8 are specified as follows:

$$\theta_v = \begin{cases} 300\,\mathrm{K}, & h < z_{mix} \\ 1.008^{(h - z_{mix})} + 299, & h \geq z_{mix} \end{cases}, \quad (2)$$

$$\overline{\theta_v}(h) = \frac{1}{h}\left[\theta_s z_{mix} + 299(h - z_{mix}) + \frac{1.008^h - 1.008^{z_{mix}}}{1.008^{z_{mix}} \ln(1.008)}\right], \quad \text{and} \quad (3)$$

$$U(h) = nh + U_s, \quad (4)$$

where $n = 0.0441$ for the stronger-shear case, $n = 0.0294$ for the weaker-shear case, and U_s is the surface wind speed set to zero. Substitution of Eqs. (2)–(4) into Eq. (1) gives

$$\mathrm{Ri}_b = \frac{g[1.008^{(h - z_{mix})} + 299 - \theta_s](h - z_{mix})}{\frac{1}{h}\left[\theta_s z_{mix} + 299(h - z_{mix}) + \frac{1.008^h - 1.008^{z_{mix}}}{1.008^{z_{mix}} \ln(1.008)}\right][n(h - z_{mix})]^2}. \quad (5)$$

The important conclusions from Fig. 8c are that 1) Ri_{crit} for both cases of chosen vertical shear corresponds to values roughly between 0.05 and 0.45 in the lowest portion of the entrainment zone (near and slightly above 350 m) that immediately surmounts the mixed layer for the two conceptualized shear magnitudes; 2) holding the Richardson number constant (as would be done for the selection of a *critical* Richardson number) for a strengthening vertical-shear magnitude corresponds to a deeper simulated PBL, effectively representing the effects of vertical-shear-driven eddies in enhancing PBL depth; and 3) increasing Ri_{crit} for a given shear profile can substantially increase the mixing depth.

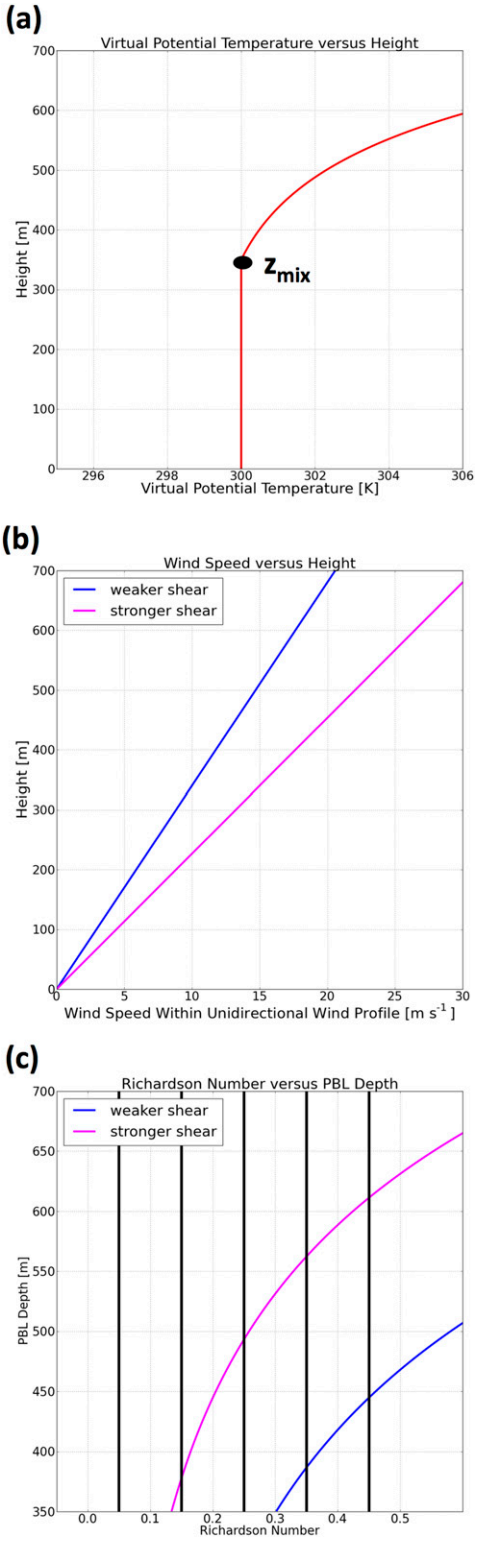

FIG. 8. (a) The vertical profile of virtual potential temperature used for conceptualizing a theoretical Richardson number profile for varying vertical shear magnitudes. In this case, the mixed layer extends from the ground to 350 m above ground, above which an exponential function describes the vertical variability of virtual potential temperature with height to 700 m. The height of the top of the mixed layer is denoted by z_{mix}. (b) Plotted are vertical profiles of wind speed for a theoretical unidirectional wind profile for two magnitudes of vertical shear: weaker (blue) and stronger (pink). The weaker-shear case corresponds to a gain of 10.3 m s^{-1} of wind speed with increasing height above the ground from the surface to the top of the mixed layer, and the stronger-shear case corresponds to a gain of 15.4 m s^{-1} in that same layer. (c) Plotted are vertical profiles (in terms of PBL depth h as height above ground) of Richardson number (plotted within a layer above the top of the mixed layer z_{mix}) that correspond to the vertical profile of virtual potential temperature displayed in (a) and the vertical profile of wind speed displayed in (b). These Richardson number profiles vary based on the strength of the vertical shear depicted in (b) and follow the relationship mathematically represented by Eq. (1): $\mathrm{Ri}_b = \{g[\theta(h) - \theta_s](h - z_{mix})\}/\overline{\theta_v}[U(h) - U(z_{mix})]^2$. Thick vertical lines indicate the different critical Richardson numbers evaluated using the ACM2 scheme as the simulated framework (ACM variation in parentheses in the following): 0.05 (ACM05), 0.15 (ACM15), 0.25 (ACM2), 0.35 (ACM35), and 0.45 (ACM45).

5. Statistical analysis

Model soundings are compared to RUC/SFCOA soundings at sounding locations, providing an opportunity for model evaluation based on particular RUC/SFCOA parameter-magnitude groupings that are treated as ''observations'' or ''actual'' values, though it is acknowledged that they contain model-related biases as stated above. This addresses the following question: ''How well do PBL schemes reproduce analyzed SECOLD thermodynamic and kinematic regimes?'' This question is answered using three procedures of statistical analysis, as subsequently described.

First, Theil's inequality coefficient U (e.g., Theil 1961, 1966; Clements and Frenkel 1980; Pindyck and Rubinfeld 1981; Trnka et al. 2006), described by CCCB15, is used to assess model performance among the nine PBL parameterizations. The definition of U is as follows:

$$U = \frac{\sqrt{\frac{1}{T}\sum_{t=1}^{T}(Y_t^s - Y_t^a)^2}}{\sqrt{\frac{1}{T}\sum_{t=1}^{T}(Y_t^s)^2} + \sqrt{\frac{1}{T}\sum_{t=1}^{T}(Y_t^a)^2}}, \tag{6}$$

where Y_t^s represents forecasts and Y_t^a represents observations. In addition, U represents normalization of the root-mean-square error, allowing for parameters whose magnitudes vary relatively widely among one another to be compared in a standardized manner (CCCB15). The

range of U values is 0 (perfect forecast) to 1 (worst possible forecast). CCCB15 also refer to the bias component of error U_m, which measures the degree of systematic model error by comparing the simulation mean over the 21 cases to the mean from the RUC/SFCOA dataset. The definition of U_m is as follows:

$$U_m = \frac{(\overline{Y}^s - \overline{Y}^a)^2}{\frac{1}{T}\sum_{t=1}^{T}(Y_t^s - Y_t^a)^2}, \tag{7}$$

where Y_t^s represents forecasts and Y_t^a represents observations. The quantity U_m measures the degree of systematic error inherent in the simulation results by comparing the overall simulation mean to the overall actual mean. The range of U_m values is 0 (no bias) to 1 (large bias). Pindyck and Rubinfeld (1981) suggest that U_m values over 0.1 denote appreciable systematic bias, necessitating adjustments to the model for its improvement. By comparing U and U_m across different PBL schemes, one can determine the relative degree of forecast error for each PBL scheme and evaluate how much of that is systematic. The reader is referred to CCCB15 for more details on U and U_m.

To supplement the above metrics, interquartile ranges (IQRs), median values, and mean parameter values over RUC/SFCOA distributions are compared with those statistics corresponding to each of the PBL schemes. These statistics therefore combine information corresponding to four sounding sites for each of the 21 cases. This permits the analysis of overall differences between simulation results using the different PBL schemes and RUC/SFCOA. This analysis is related to the computation of the U_m statistic in that it provides a sense of overall bias, and this analysis also provides the sign of the overall bias. Furthermore, these comparisons are decomposed into diurnal and nocturnal components, such that distributions are created for separate 1300–0000 UTC and 0100–1200 UTC time periods, respectively. These results are presented in both integrated and bulk form to highlight some of the more apparent, overarching differences between the PBL schemes and the RUC/SFCOA dataset. While these differences are not investigated in detail (e.g., decomposition of individual variables into various components and analysis thereof), the purpose of the present work is to highlight the behavioral tendencies of PBL schemes relevant to evaluating their performance in the SECOLD regime for basic meteorological variables. This is intended to satisfy the operational meteorologist's interest in identifying aspects of model biases, and the theoretician's interest in identifying the relationships between the design of PBL schemes and their performance and motivating future research to investigate more intricate details of physical processes and interactions that are ongoing in these simulations (e.g., surface fluxes).

The Kolmogorov–Smirnov (K–S) test (Massey 1951) is used to statistically test the differences between the different PBL schemes and RUC/SFCOA. The K–S test compares the differences between the cumulative density functions corresponding to two samples, and here compares the parameter distributions provided by different PBL schemes to those from RUC/SFCOA. Larger differences in the cumulative density function with increasing parameter values correspond to the greater likelihood that the two samples are from different populations (lower p values). The K–S test is nonparametric, which is a strength of this statistical approach owing to its lack of a distribution assumption. However, results from this test can be sensitive to both large sample sizes and differences between cumulative density functions that may only occupy relatively small portions of the full ranges of the distribution values. Values of p below 0.05 (statistically significant) are distinguished from those between 0.05 and 0.10 (marginally statistically significant) and those above 0.10 (not statistically significant).

This section concludes with an analysis of the validity of the RUC/SFCOA dataset based on a comparison to observed soundings. This is accomplished by the consideration of multiple variables, as subsequently discussed.

a. 0–3-km lapse rate

Theil's inequality coefficient U for 0–3-km lapse rate is relatively similar among all PBL schemes, although slightly lower for ACM2 (nonlocal–local) and its variants, along with the YSU (nonlocal) scheme, which also minimizes the bias component U_m (Fig. 9). Local schemes (MYJ and QNSE) exhibit the largest bias component U_m.

For both diurnal and nocturnal distributions, local schemes (MYJ and QNSE) consistently produce statistically significantly smaller low-level lapse rates compared to nonlocally influenced schemes (ACM2 and its variants, along with the MRF and YSU schemes) (Fig. 10). This underforecast by the local schemes is accentuated at night, when the background statically stable conditions are encouraged by nocturnal cooling of the surface layer. Nonlocally influenced schemes do not demonstrate substantial low biases between both diurnal and nocturnal periods, when comparing mean values and IQRs for simulations and RUC/SFCOA distributions (Figs. 9 and 10), though the MRF and YSU schemes provide high biases at night. In fact, IQRs and

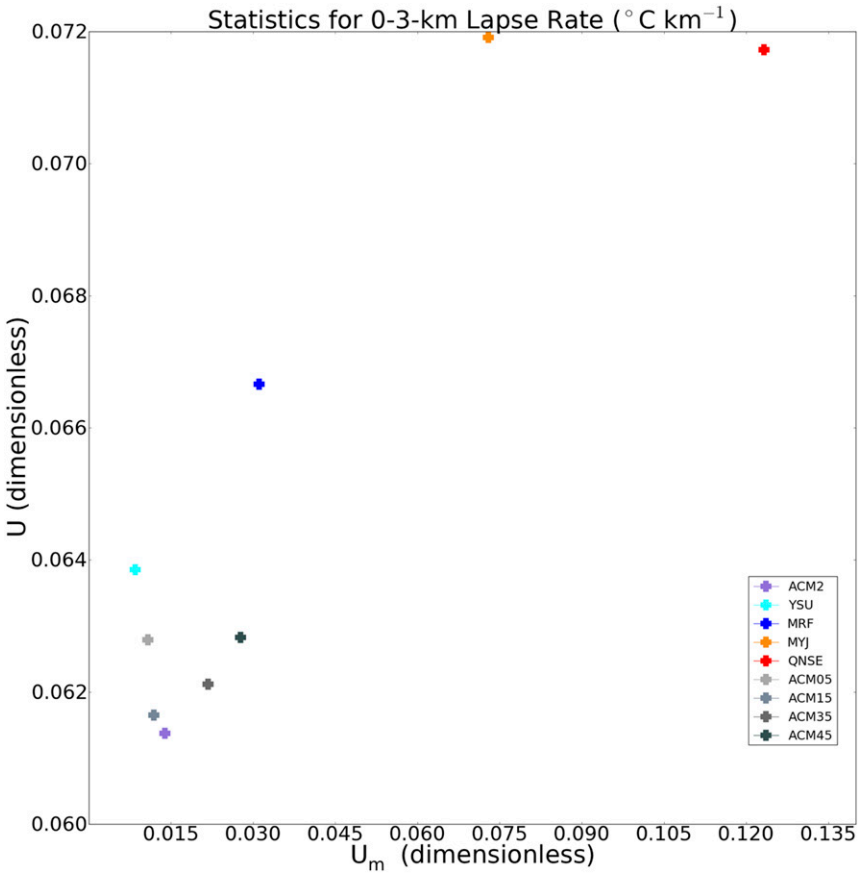

FIG. 9. Scatterplot of Theil's inequality coefficient U vs bias component of error U_m for 0–3-km lapse rate. Each marker corresponds to each PBL parameterization scheme, with markers color coded based on PBL scheme type and identified in the legend in the bottom-right part of the figure. Vertical and horizontal axes are scaled equivalently for this and all subsequent scatterplots of U vs U_m to permit relative comparisons of error and its bias component (i.e., U and U_m values closer to 0 indicating less error and a lesser bias component, respectively). Blue colors correspond to nonlocal schemes, orange/red colors correspond to local schemes, and purple/gray colors correspond to hybrid nonlocal–local schemes.

mean values for simulations come close to matching those for the RUC/SFCOA in several instances for the nonlocally influenced schemes. This suggests the necessity of incorporating nonlocal PBL scheme design to avoid systematic underestimations of low-level lapse rates.

b. *Mean lowest-100-mb mixing ratio*

The lowest-100-mb mean mixing ratio (Fig. 11; 1 mb = 1 hPa) is relatively well forecast by all PBL schemes in comparison to the 0–3-km lapse rate (Fig. 9), though the ACM2 scheme and its variants do indicate statistically significantly more moist conditions during the diurnal period (Fig. 12). Except for the MRF scheme, U_m values are below 0.1, consistent with the generally limited bias component for the simulations (Fig. 11). There is a relatively small overforecast for all schemes except local ones (Fig. 12), which is most apparent for the MRF scheme, based on comparisons of mean values and IQRs for simulation distributions to RUC/SFCOA distributions.

c. *Planetary boundary layer depth*

PBL depth is a measure of how deep the vertical turbulent mixing is simulated using the different PBL parameterizations. To apply a consistent method of determining PBL depths across the different PBL parameterizations and the RUC/SFCOA soundings, the methodology of Coniglio et al. (2013) is used in assessing PBL depth, which is based on methods created by developers of the RUC to derive a PBL-top variable. The PBL top is the first level above where the virtual

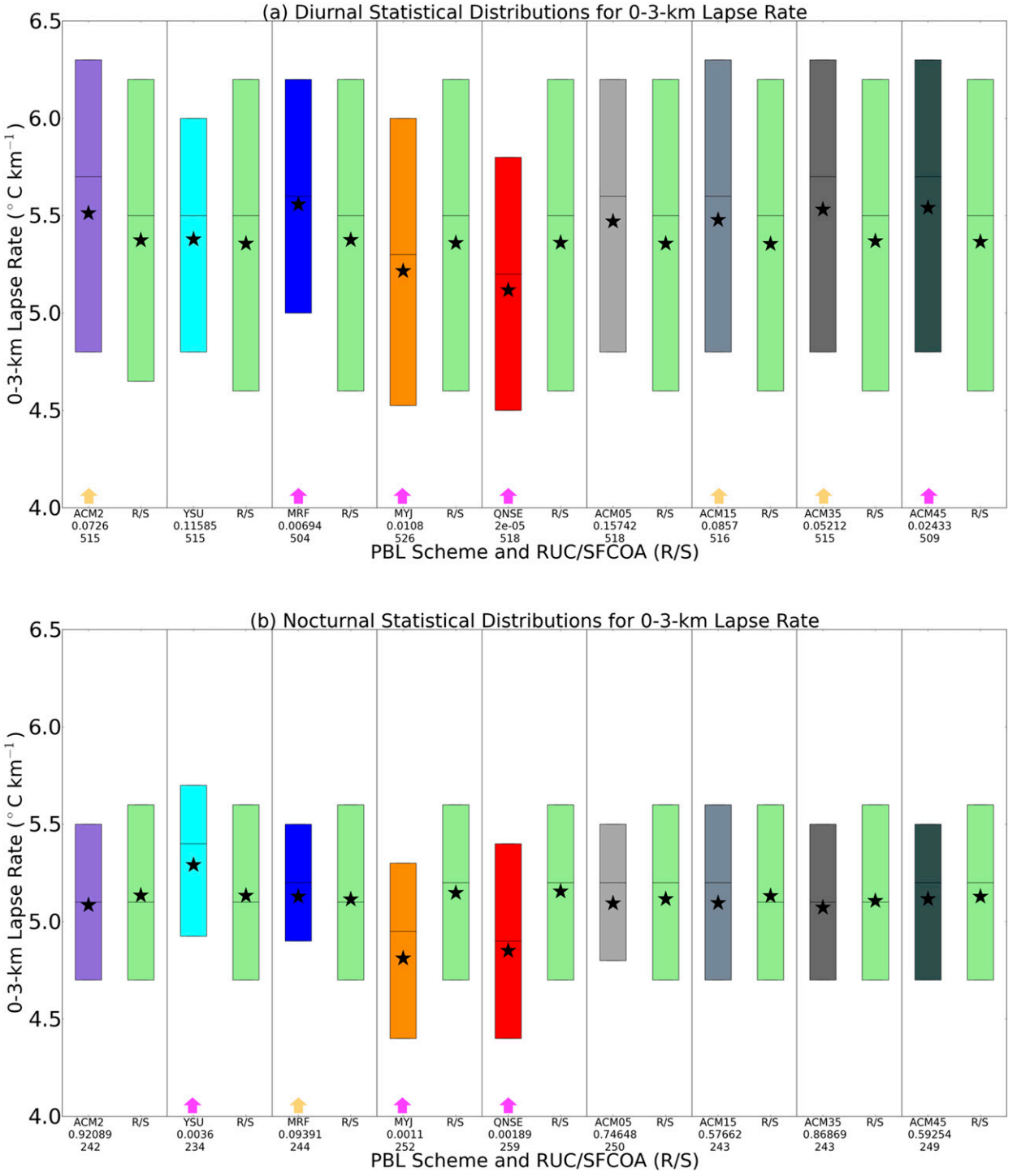

FIG. 10. IQR (color coded), median value (black horizontal line), and average value (black star) for each PBL scheme for the 0–3-km lapse rate. Color coding for PBL schemes is as in Fig. 9. Simulation results (green) representing the RUC/SFCOA (R/S) soundings depict the IQR, median value (black horizontal line), and average value (black star). The p value corresponding to the K–S test between the PBL scheme distribution and the R/S distribution is listed below the PBL scheme label (rounded and expressed to as many as five decimal places, including the use of exponential notation for p values with zeros in at least the first four decimal places), below which the distribution sample size is provided. The p values < 0.05 (statistically significant) are indicated by a magenta up arrow, p values between 0.05 and 0.10 (marginally statistically significant) are indicated by a dark-yellow up arrow, while no arrow is provided for p values > 0.10. (a) Statistics for the diurnal subset of the 0–3-km lapse rate dataset from 1300 UTC through 0000 UTC; and (b) as in (a), but for the nocturnal subset from 0100 through 1200 UTC.

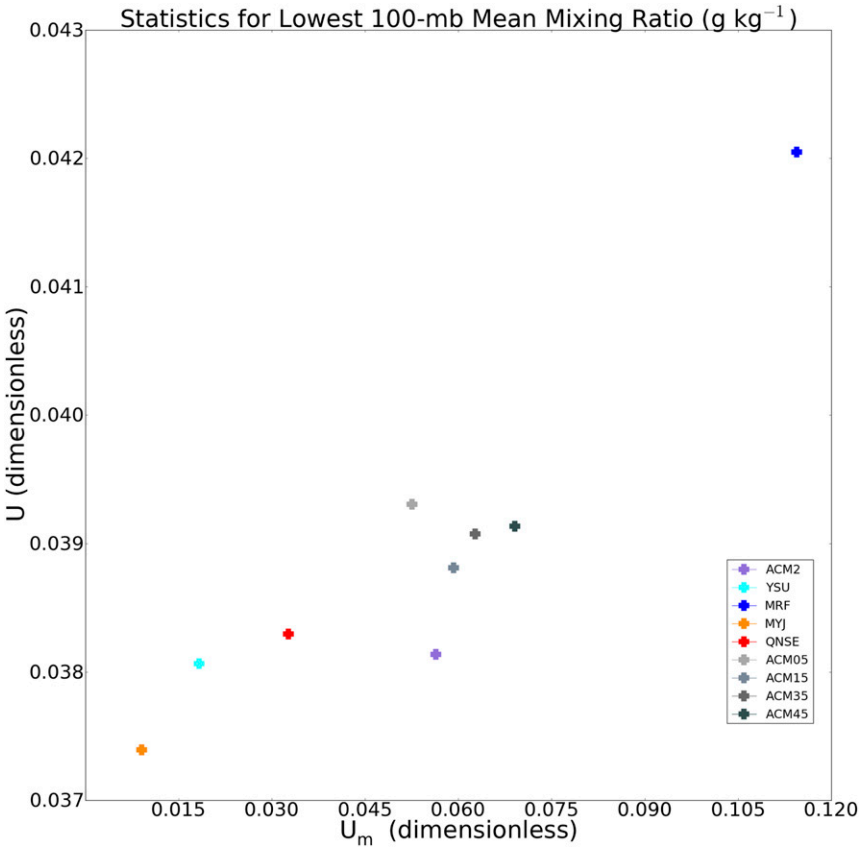

FIG. 11. As in Fig. 9, but for the mean mixing ratio in the lowest 100 mb. Note that the *x*- and *y*-axis ranges differ from those in Fig. 9.

potential temperature exceeds the maximum virtual potential temperature in the lowest three levels by more than 0.6 K.

There is a large bias component (underforecast) in PBL depth (Fig. 13) for the local PBL schemes, with this bias component being characterized by an underforecast (Fig. 14), with relatively greater error for the MYJ (local) and QNSE (local) schemes, similar to 0–3-km lapse rate (Fig. 9). Minimization of both error and its bias component come from using the ACM2 (nonlocal–local) scheme and its variants, along with the YSU (nonlocal) scheme, with all of these schemes representing nonlocally influenced mixing.

During the day, the simulated PBL depth is underforecast based upon simulated mean and 50th- and 75th-percentile values, using the local MYJ and QNSE schemes (Fig. 14). Nonlocal schemes do not provide similar underforecasts. The ACM2 and its variants simulate deeper PBLs compared to RUC/SFCOA output based upon mean values and IQRs, though this overforecast is relatively lessened when using the ACM05 scheme (similar to 0–3-km lapse rates being better forecast by the ACM05). These findings are consistent with much of the previous literature regarding the depiction of deeper mixing using nonlocal PBL parameterization schemes (e.g., CCCB2015; Coniglio et al. 2013; Stensrud 2007). In the case of the SECOLD regime, it is clear that local schemes provide unrealistically shallow PBLs. Furthermore, relatively larger simulated PBL depths are associated with relatively larger $\mathrm{Ri_{crit}}$ for the variants of the ACM2 (nonlocal–local) scheme, particularly during diurnal periods (Fig. 14), though a one-to-one relationship between PBL depth and exact $\mathrm{Ri_{crit}}$ values is not evident.

The notion that the ACM2 (nonlocal–local) variants associated with higher critical Richardson numbers yield the deepest PBLs is consistent with the earlier hypothesis that these higher thresholds would be achieved at a higher level above the ground. This would particularly be the case in an environment characterized by strong vertical shear. In the more strongly sheared environment, the environmental Richardson number is relatively lower, representing enhanced turbulence, and

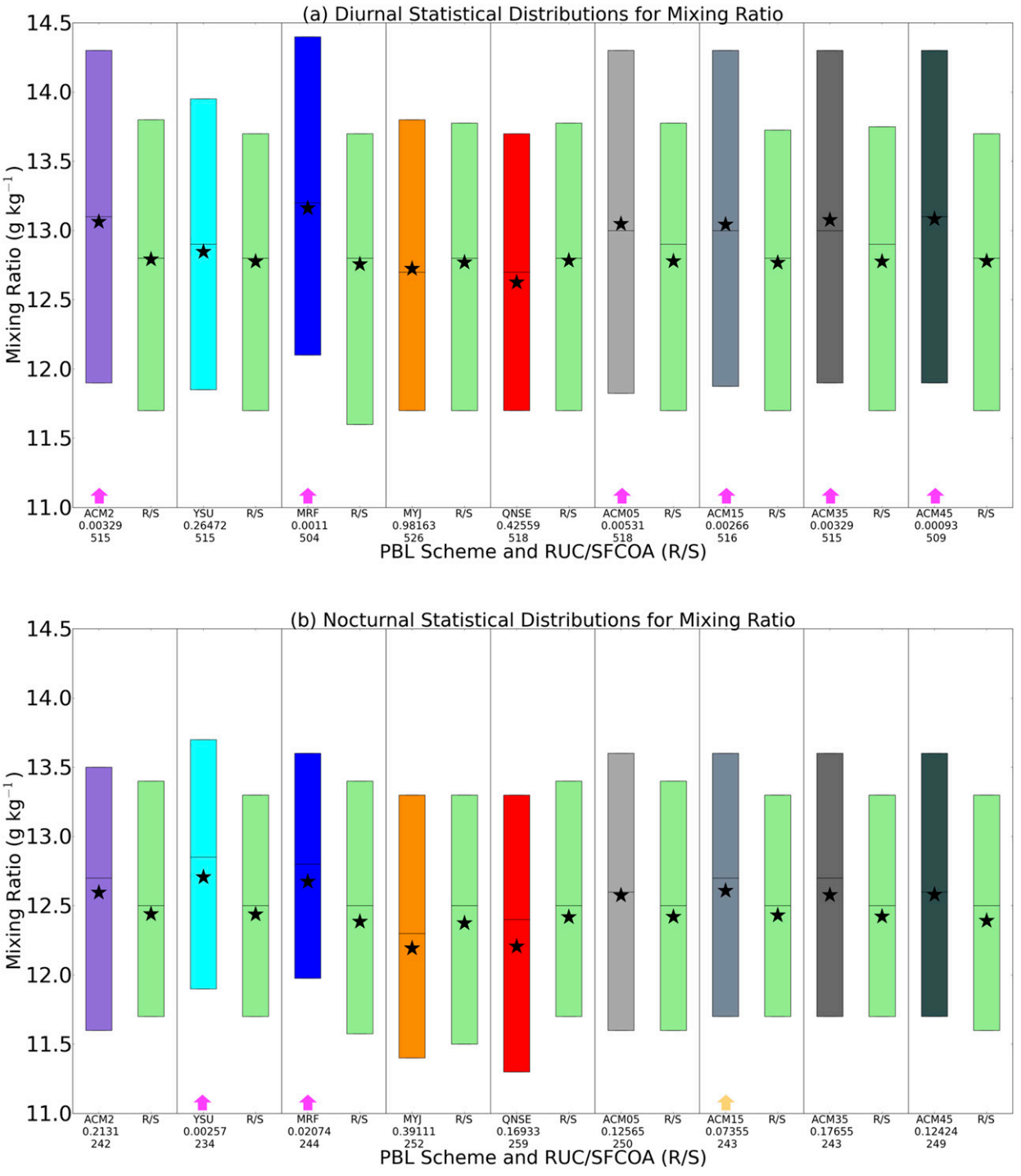

FIG. 12. As in Fig. 10, but for mean mixing ratio in the lowest 100 mb.

simulated strong vertical mixing must extend through a deeper layer of the troposphere to reach a particular Ri_{crit} value. Accordingly, the increasing vertical wind shear is physically associated with strengthened vertical mixing and a deeper PBL related to the mechanical production of turbulence. At the same time, increasing the Ri_{crit} value directly accounts for further amplification of the simulated PBL depth in the strongly sheared, SECOLD environment, such that the degree to which mechanical-turbulence-enhanced vertical

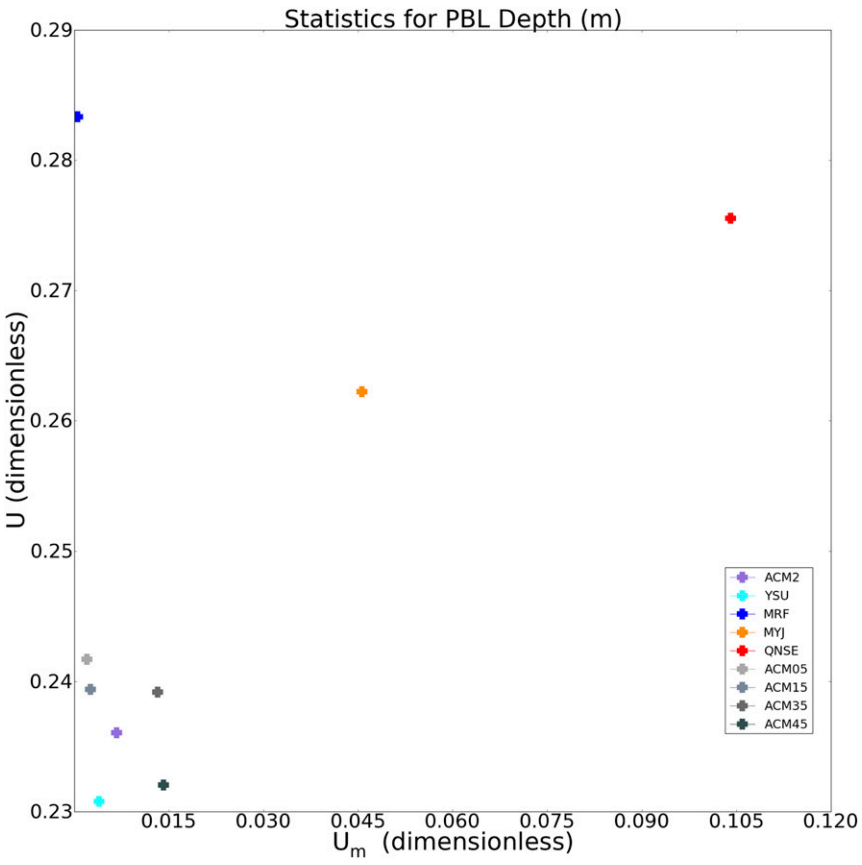

FIG. 13. As in Fig. 9, but for PBL depth. Note that the *x*- and *y*-axis ranges differ from those in Fig. 9.

mixing amplifies the PBL depth is best suited for relatively higher Ri_{crit} values to produce smaller U values. To what degree this PBL-depth amplification should be represented in the SECOLD regime in numerical simulations was previously unknown, and this Ri_{crit} experiment validates the relationship between such variability and simulated PBL depth in the SECOLD regime.

At night, most schemes offer too-shallow PBL depths based on comparisons to RUC/SFCOA output. However, the local MYJ and QNSE schemes produce slightly shallower PBLs compared to the other schemes that include nonlocal influences. One exception is the nonlocal YSU scheme, which simulates an average and IQR for PBL depth greater than that for RUC/SFCOA. Of note, the aforementioned nocturnal PBL depth calculations likely reflect the depth of the nocturnal boundary layer (NBL; e.g., Güldner and Spänkuch 2001), which can be distinguished from a deeper PBL. This difference and its variability among simulations using different PBL parameterization schemes could be foci for future research. Future research could also identify relationships between lapse rate profiles and properties of the boundary layer at night, perhaps through an investigation of the components of the lapse rates (i.e., temperatures at specific levels in the vertical profile used to derive the lapse rates).

d. Mixed-layer convective available potential energy

Theil's inequality coefficient suggests that MLCAPE is poorly forecast using all PBL parameterization schemes, when compared to RUC/SFCOA soundings (Fig. 15). There is a consistent signal for all PBL schemes to statistically significantly overforecast MLCAPE relative to the RUC/SFCOA dataset during both diurnal and nocturnal periods (Fig. 16). This motivates the need to analyze the potential systematic biases for integrated buoyancy in the RUC/SFCOA dataset. The use of 0–3-km lapse rates does demonstrate utility in assessing the potential for significantly severe storms (Sherburn and Parker 2014) and could be used as another indicator of the thermodynamic environment to assess background instability. There does appear to be a slight decrease in simulated MLCAPE and decrease in positive bias with increasing

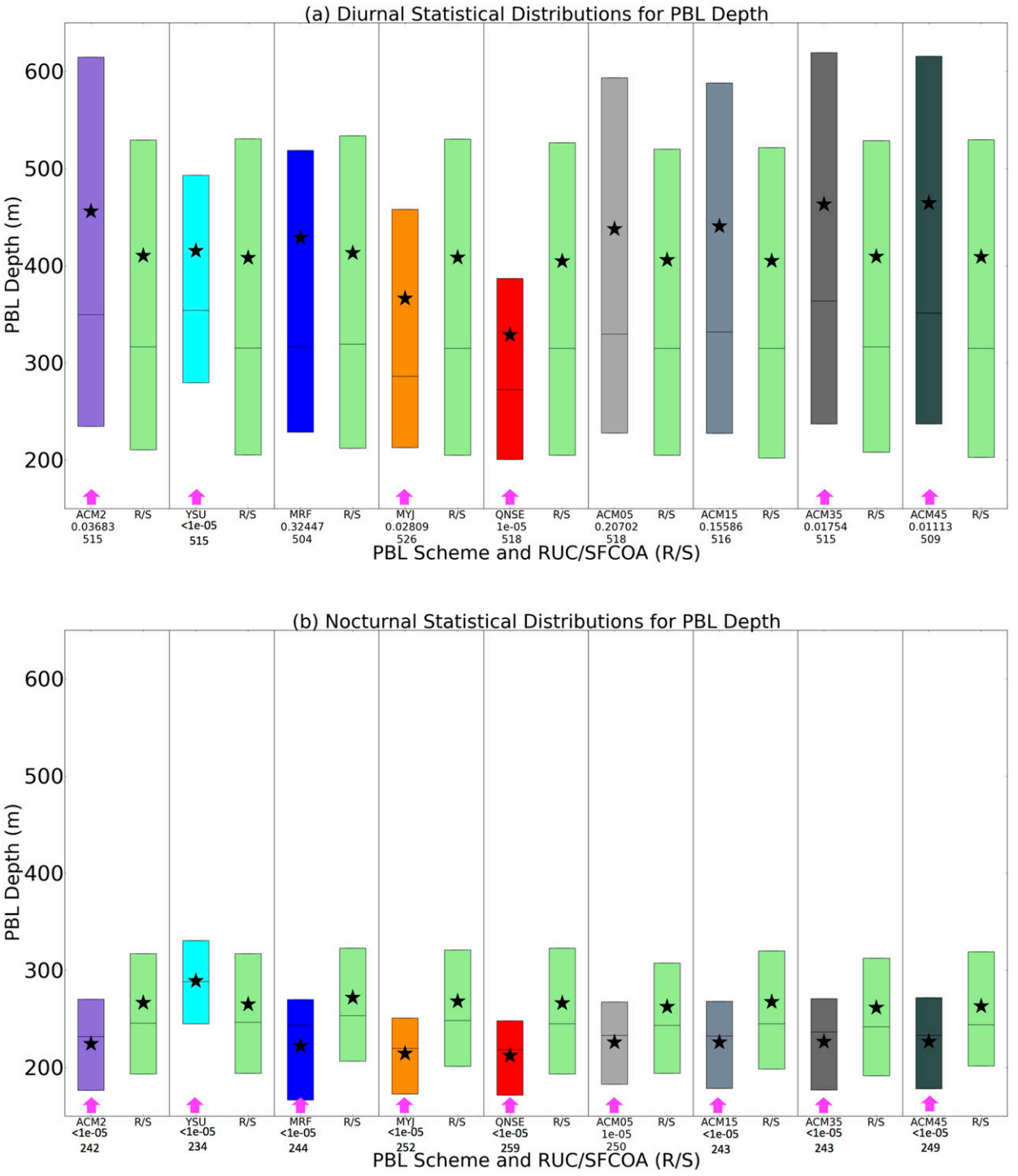

FIG. 14. As in Fig. 10, but for PBL depth.

Ri_{crit} among the ACM2 (nonlocal/local) scheme and its variants. However, given the integrated nature of MLCAPE and its incorporation of not only the temperature, but also moisture, distributions, it would be highly speculative to relate Ri_{crit} variability with MLCAPE variability. Ultimately, this encourages further research to investigate the sensitivity of the SECOLD environment to simulated integrated buoyancy, as well as estimates of CAPE from RUC/SFCOA versus observational data sources.

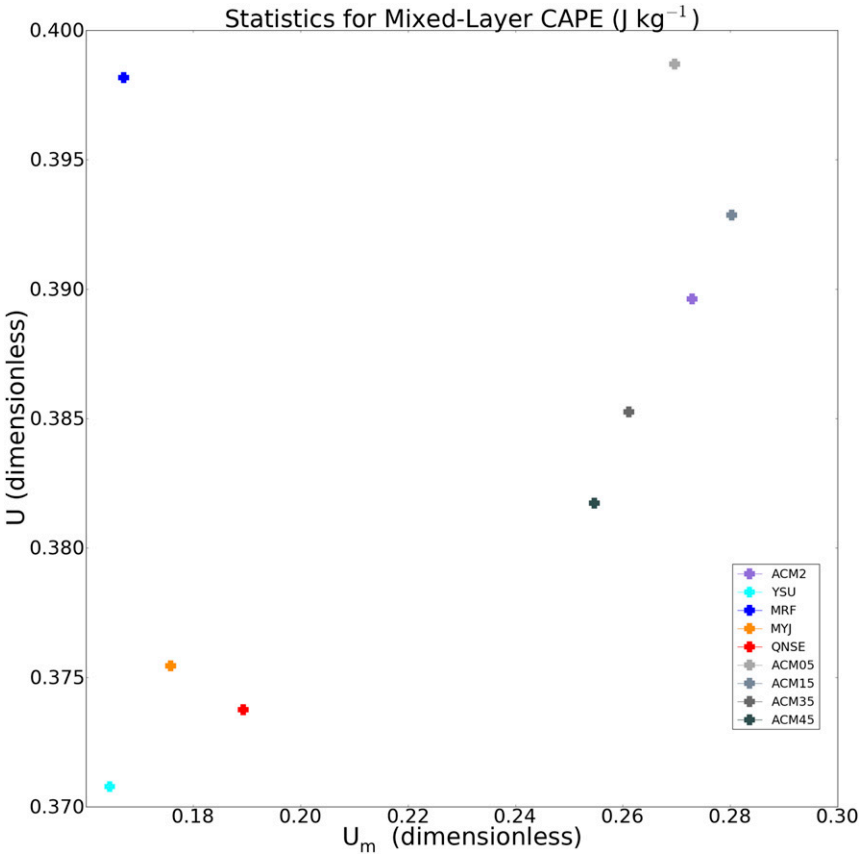

FIG. 15. As in Fig. 9, but for MLCAPE. Note the *x*- and *y*-axis ranges differ from those in Fig. 9.

e. 0–3-km storm-relative helicity

Theil's inequality coefficient for 0–3-km SRH (Fig. 17) reveals relatively similar error for all PBL schemes for 0–3-km SRH, though the results are slightly lower for the MYJ (local) and QNSE (local) schemes and the ACM2 (nonlocal–local) schemes and its variants. The ACM2 (nonlocal–local) scheme and its variants represent an intermediate zone for the bias component of error, lying between the nonlocal schemes with a greater bias component and the local schemes with a lesser bias component. Simulation bias for 0–3-km SRH is lowest using the MYJ (local) and QNSE (local) schemes and is highest for the nonlocally influenced schemes (Fig. 17). Furthermore, the YSU and MRF nonlocal schemes exhibit the lowest SRH (statistically significantly lower than RUC/SFCOA distributions), based on average values and IQRs (Fig. 18) especially during the nocturnal period. This is consistent with nonlocal schemes depicting deeper PBLs, which contain greater vertical mixing of momentum and lower SRH compared to strictly local schemes. The local (MYJ and QNSE) schemes indicate generally higher SRH, though with a trend toward underforecasting at night.

Comparing Fig. 17 with Fig. 9 and Fig. 13, it is evident that local schemes offer the greatest bias component for 0–3-km lapse rate and PBL depth, whereas nonlocal schemes offer the greatest bias component for 0–3-km SRH. Meanwhile, the ACM2 (nonlocal–local) and its variants lower the bias component for all of these parameters from the most extreme bias-component magnitudes for a given parameter (cf. Fig. 17 with Fig. 9 and Fig. 13).

f. Comparisons of RUC/SFCOA soundings to observed soundings

Throughout the aforementioned discussion, the RUC/SFCOA dataset is treated as the observationally influenced dataset for generating consistent comparisons to observations. As previously mentioned, the SFCOA system is considered to be the standard for real-time, mesoscale analysis, substantiating its use as a comparison dataset in the present study. In this section, a cursory attempt at identifying biases in the RUC/SFCOA

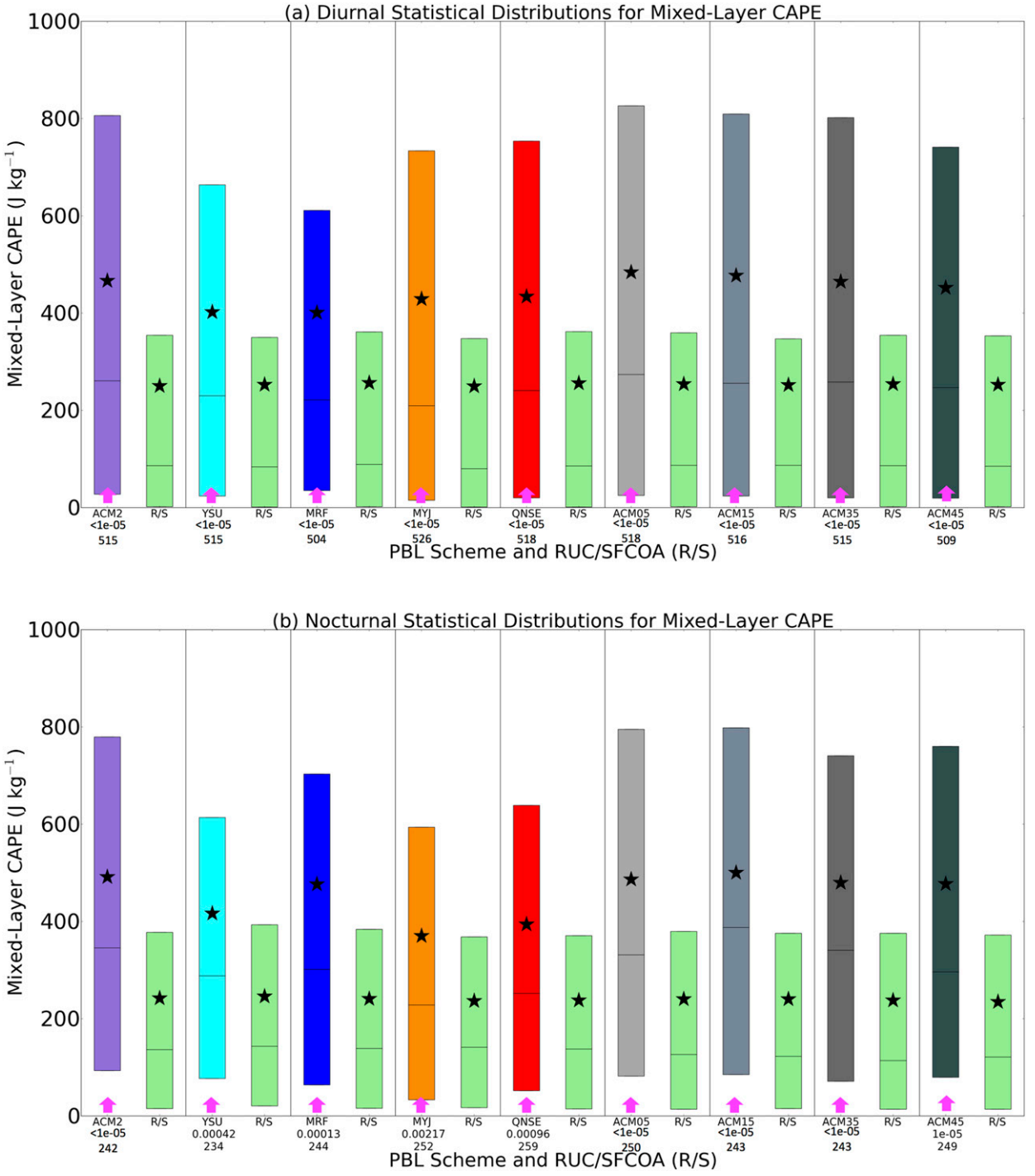

FIG. 16. As in Fig. 10, but for MLCAPE.

dataset is performed, through comparisons of the RUC/SFCOA to observed soundings.

Among the events and locations illustrated in Figs. 5–7, RUC/SFCOA grid points that were also the nearest grid points to observed sounding locations serve as the basis for subsequent analysis. These locations include Jackson, Mississippi; Birmingham, Alabama; Peachtree City, Georgia; and Lake Charles, Louisiana. A total of 13 selected RUC/SFCOA grid points were also in closest proximity to observed sounding locations for analysis, with up to three observed–simulated sounding comparisons permitted: 1200 UTC followed by 0000 UTC and

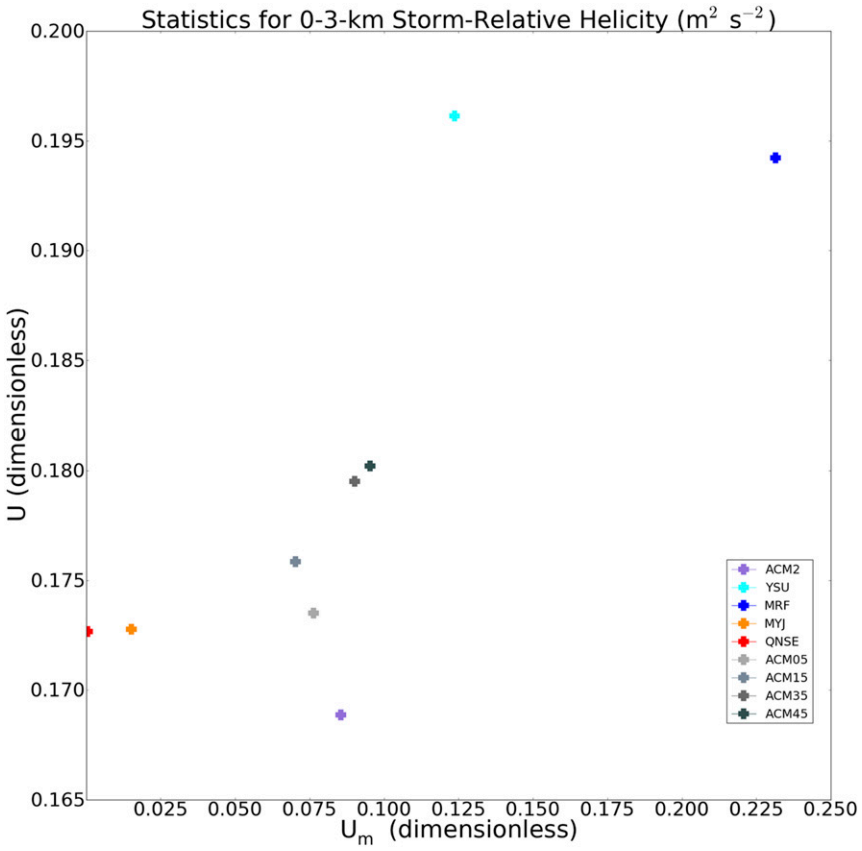

FIG. 17. As in Fig. 9, but for 0–3-km SRH. Note that the *x*- and *y*-axis ranges differ from those in Fig. 9.

then 1200 UTC spanning 24-h analyses. This yields a total of 38 RUC/SFCOA soundings compared against observed soundings (1 potential sounding comparison is not permitted because of a lack of archived data, precluding 39 comparisons), from which moisture, lapse rate, buoyancy, and storm-relative helicity are calculated.

Differences between RUC/SFCOA and observed soundings are computed for several parameters as illustrated in Fig. 19: CAPE and convective inhibition (CIN) corresponding to the most unstable parcel (MUCAPE and MUCIN) in Fig. 19a, lowest-100-mb mean mixing ratio (MIXR), precipitable water (PW) in Fig. 19b, lapse rates (LR) in the 0–3-km and 700–500-mb layers (0–3-km LR and 700–500-mb LR) in Fig. 19c, and SRH in the 0–1-km and 0–3-km layers in Fig. 19d. Figure 19 highlights biases in the RUC/SFCOA dataset. An apparent low-buoyancy and dry bias are evident in the RUC/SFCOA dataset. This is especially apparent in the analysis of MUCAPE and PW. In fact, the lower bounds of the interquartile range for RUC/SFCOA–observation differences for MUCAPE and PW are more negative than $-100\,\mathrm{J\,kg^{-1}}$, and 0.8 in., respectively. RUC/SFCOA–observation differences for lapse rate and SRH are relatively more centered around zero. While this represents only a cursory investigation of RUC/SFCOA soundings in representing the true atmosphere, it does highlight some potential biases evident in this dataset, which could be the focus of future research. Nevertheless, given the spatiotemporal regularity of SFCOA, an understanding of PBL scheme performance relative to the RUC/SFCOA dataset is critical to a consistent interpretation of model output for operational meteorology. It is noteworthy that there are some cases of RUC/SFCOA biases (based on observed soundings) illustrated in Fig. 19 that overwhelm the simulation–RUC/SFCOA differences (Figs. 10, 12, 14, 16, and 18). This does cast some degree of doubt on the precise magnitudes of simulation bias implied by these figures. However, these figures do highlight general behavioral tendencies of the differences between simulated quantities and RUC/SFCOA estimates of the real atmosphere, to be considered in relative terms.

The preceding analysis of differences between RUC/SFCOA soundings and observed soundings in the SECOLD environment could serve as the foundation

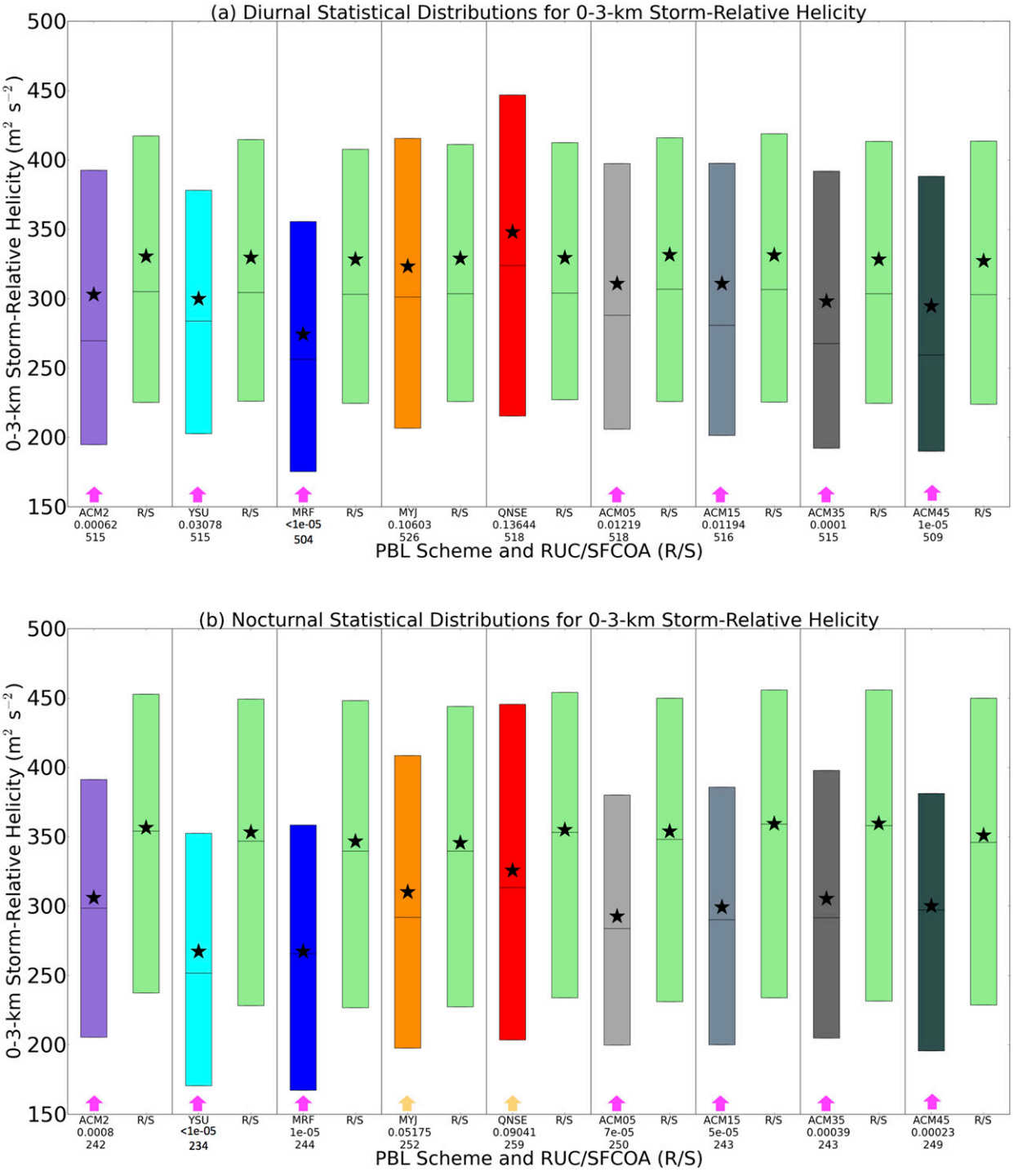

FIG. 18. As in Fig. 10, but for 0–3-km SRH.

for subsequent investigation of other input components to this study, such as an analysis in the errors in initial and boundary conditions. However, it is anticipated that substantial additional research would need to be performed to fully evaluate the validity of inputs and assumptions used in the WRF simulations. This is the case given the overwhelmingly large sample size of soundings considered in this study among multiple cases and many locations, given long-duration (24 h) forecast cycles influenced by many other factors aside from

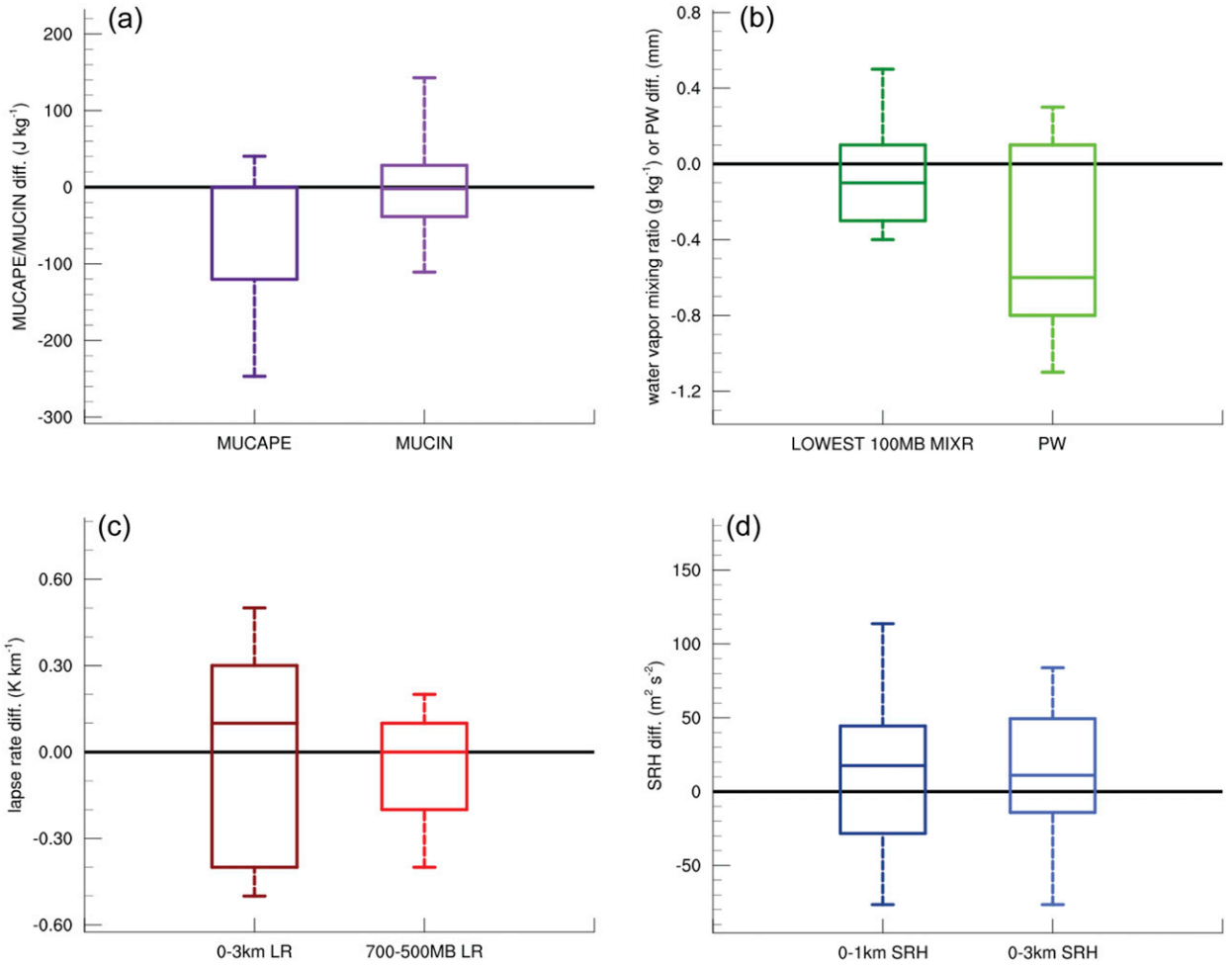

FIG. 19. Differences (diff.) between parameters calculated from R/S and observed soundings (observed sounding parameters subtracted from R/S parameters): (a) MUCAPE and MUCIN, (b) lowest-100-mb mean mixing ratio (LOWEST 100MB MIXR) and PW, (c) 0–3-km LR and 700–500-mb LR, and (d) 0–1- and 0–3-km SRH. Each box denotes the IQR, with the median indicated by an embedded horizontal line (except for MUCAPE, where the median and 75th-percentile markers overlap). Dashed lines extend outward to the 10th and 90th percentiles.

initial and boundary conditions such as the PBL and other parameterization schemes. The analysis of RUC/SFCOA biases provided herein offers an attempt to investigate assumptions inherent to critical inputs.

6. Convective morphology sensitivity

CCCB15 provide a cursory overview of the sensitivity of simulated convective morphology to the selected PBL scheme; differences in the environmental conditions influenced by the choice of the PBL ultimately yield differences in the morphological characteristics of the depicted convective processes. These differences can be manifested in the operational forecaster's assessment of the severe weather risk and are an important consideration of the validity of a model solution. A complete evaluation and comparison of convective attributes simulated using the nine PBL schemes addressed in this manuscript are outside its scope. However, a cursory investigation of differences among simulated convective processes is performed.

Plan-view depictions of simulated composite reflectivity produced for all nine PBL schemes for each of the 21 cases were reviewed to subjectively identify differences in the timing, location, mode, and intensity of convection, between separate schemes and between these schemes and observed composite radar reflectivity. Many of the differences are seemingly subtle, and a much more extensive study would be required to accurately and precisely identify simulation differences. However, one modest signal is present for the ACM2 scheme and its variants to more consistently produce

separated, open-warm-sector convective elements, at times ahead of more linearly organized convective segments and clusters. These more separated convective elements can serve as a signal to operational forecasters that discrete or semidiscrete cells (perhaps supercells) would be favored by adequate open-warm-sector ascent, with such a convective mode offering a wide variety of potential hazards, possibly including tornadoes.

A couple of examples of the ACM2 scheme, and its variants, uniquely depicting the most spatially separated convective elements are provided in ensemble plan-view depictions are provided in Figs. 20 and 21, with white-oval annotations provided to highlight areas corresponding to subsequent discussion. Figure 20 indicates the simulation corresponding to an event consisting of a quasi-linear band of convection from the Jackson area extending southwestward to south-central Louisiana, with separated cells farther east toward the New Orleans, Louisiana, area that did produce tornadoes. The ACM2 scheme, and its variants (especially the ACM35 and ACM45), provided the best indications of an open-warm-sector separated-updraft regime displaced from the simulated cluster- and quasi-linear-mode convection. This simulated convective mode is a critical component of the simulation, despite spatial errors, as the ACM2 and its variants (especially the ACM35 and ACM45) uniquely offer an indication that cellular convection would be a concern, potentially heightening awareness among operational meteorologists that a supercell-tornado risk could occur. The same general concept is illustrated in Fig. 21 for separated convective elements from portions of central Alabama to central Georgia, which did produce tornadoes. Once again, the ACM2 scheme and its variants (especially the ACM35 and ACM45) offered the strongest signal for more separated convective elements across the general region that experienced tornadoes, though spatial errors are evident.

Similar morphological differences in simulated convection depicted in Figs. 20 and 21 are also apparent in other cases, though not shown in the present work. A more thorough analysis of the sensitivity of simulated convective morphology owing to PBL scheme selection would be a possible area of future research and would complement the analysis of environmental parameters. As a related matter, the influence of cloud coverage, its depiction, and its manifestation on PBL scheme performance could also be foci for additional research. This relates to differences in convective morphology, in the sense that differences in cloud formation and evolution as simulated by the WRF could have a marked influence on the simulated thermodynamic and kinematic profiles. The sensitivity of convective morphology, as cursorily investigated in the present work, is expected to also extend to that of cloud coverage and evolution, and this could be an avenue for future research.

7. Conclusions

As a part of a model evaluation process for the challenging southeast U.S. cold season severe weather regime, work previously introduced by CCCB15 is applied, which invokes a warm-sector-based analysis of forecast soundings compared against a RUC/SFCOA sounding dataset that incorporates observations. This permits a reproducible system for the evaluation of convection-allowing model guidance, which is relevant for operational meteorology, with the sole focus of the present work being on model performance using different PBL parameterization schemes.

Through an investigation of nine different PBL schemes—two nonlocal ones (YSU and MRF), two local ones (MYJ and QNSE), and one hybrid nonlocal–local scheme (ACM2) with four newly constructed variants by modifying Ri_{crit} (ACM05, ACM15, ACM35, and ACM45)—many distinguishable results became apparent upon comparisons to RUC/SFCOA soundings in the model evaluation process. First, for 0–3-km lapse rate and PBL depth, local schemes provide the largest differences from RUC/SFCOA as an underestimation, especially at night. For PBL depth, the smallest error and the smallest bias component correspond to the ACM2 (nonlocal–local) and its variants, along with the YSU (nonlocal) scheme. For 0–3-km SRH, strictly nonlocal schemes provide the largest mean differences from observations as an underestimation. Mean mixing ratio in the lowest 100 mb is relatively well forecast by all PBL parameterization schemes, though a slightly positive bias is exhibit by nonlocally influenced schemes, especially the MRF. For all evaluated variables except MLCAPE, the ACM2 (nonlocal–local) scheme and its variants never provide the largest simulation mean difference from RUC/SFCOA output and sometimes provide the smallest difference and error. MLCAPE is substantially overforecast by all schemes. While this encourages the general use of ACM2 and its variants, there could be specific variables and regimes for which purely local or purely nonlocal schemes would be more appropriate for use in simulations, depending on various atmospheric regimes (i.e., those outlined by CCCB15).

These results regarding nonlocal versus local versus hybrid nonlocal–local PBL parameterization schemes can be linked to previous research that demonstrates a commonality among local schemes to represent too weak vertical mixing in the PBL while nonlocal schemes overmix the PBL (e.g., CCCB15; Coniglio et al. 2013;

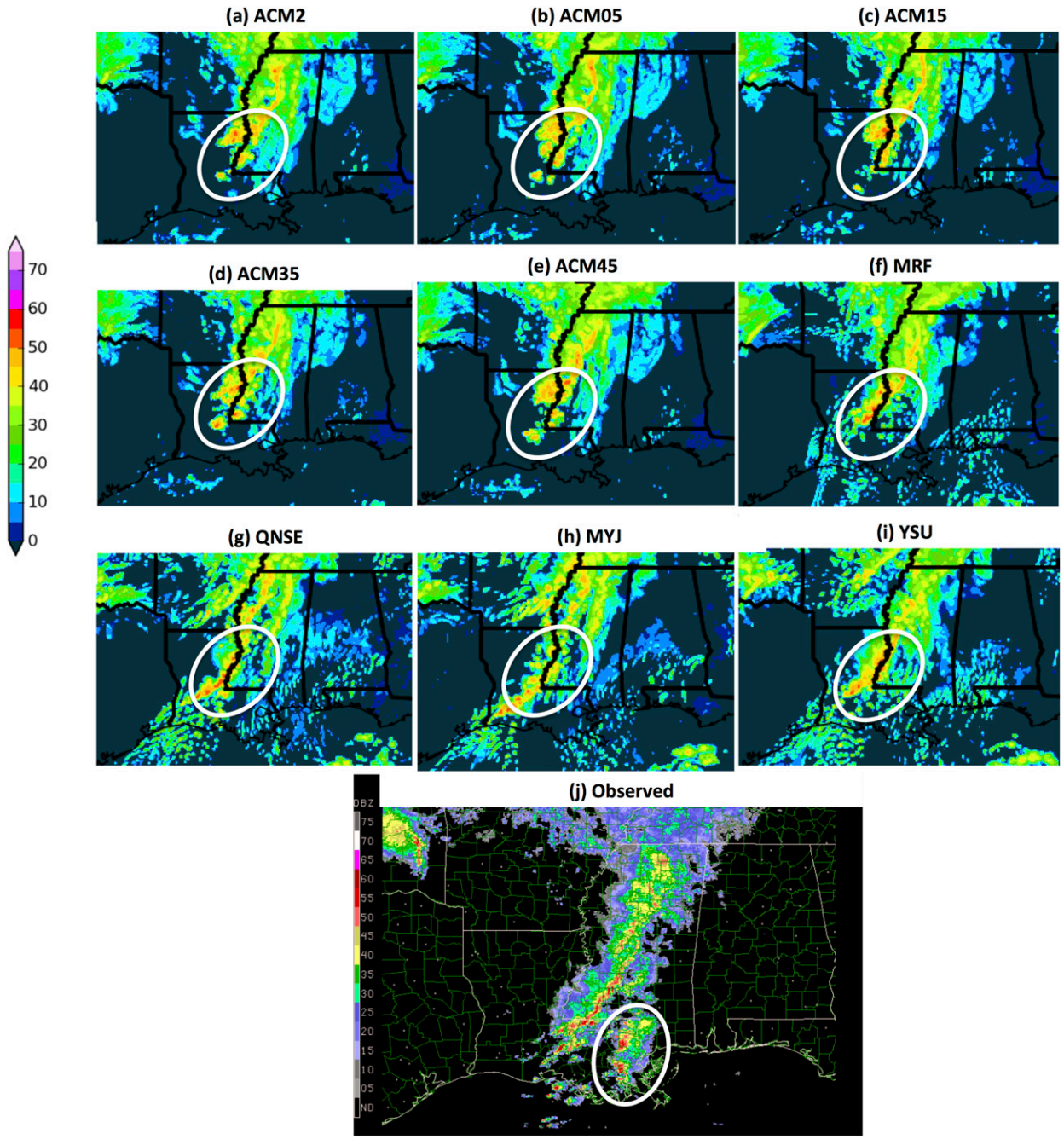

FIG. 20. (a)–(i) The 21-h forecast of simulated composite reflectivity (dBZ) for each WRF PBL member valid at 0900 UTC 13 Feb 2007 and (j) the observed mosaic composite reflectivity from the NCAR Mesoscale and Microscale Meteorology Laboratory Image Archive (NCAR 2017) at 0900 UTC 13 Feb 2007. White ovals are overlaid in the panels to indicate regions of convection referenced within the main text, relevant for differences in convective mode between simulated convection and the observations. The color scale for simulated reflectivity is somewhat different than for observed reflectivity; however, both color scales are intended to highlight more-intense precipitation with warmer colors (e.g., red, purple) and less-intense precipitation with cooler colors (e.g., blue, green) for the purpose of generalizing the convective intensity and mode.

Stensrud 2007). Meanwhile, the hybrid schemes indicate more intermediate mixing in the SECOLD regime where vertical shear enhances mixing and limited instability suppresses mixing, with some of the aforementioned biases being more muted. This is consistent with some of the improved profiles of the PBL demonstrated by using the ACM2 scheme (e.g., Pleim 2007b).

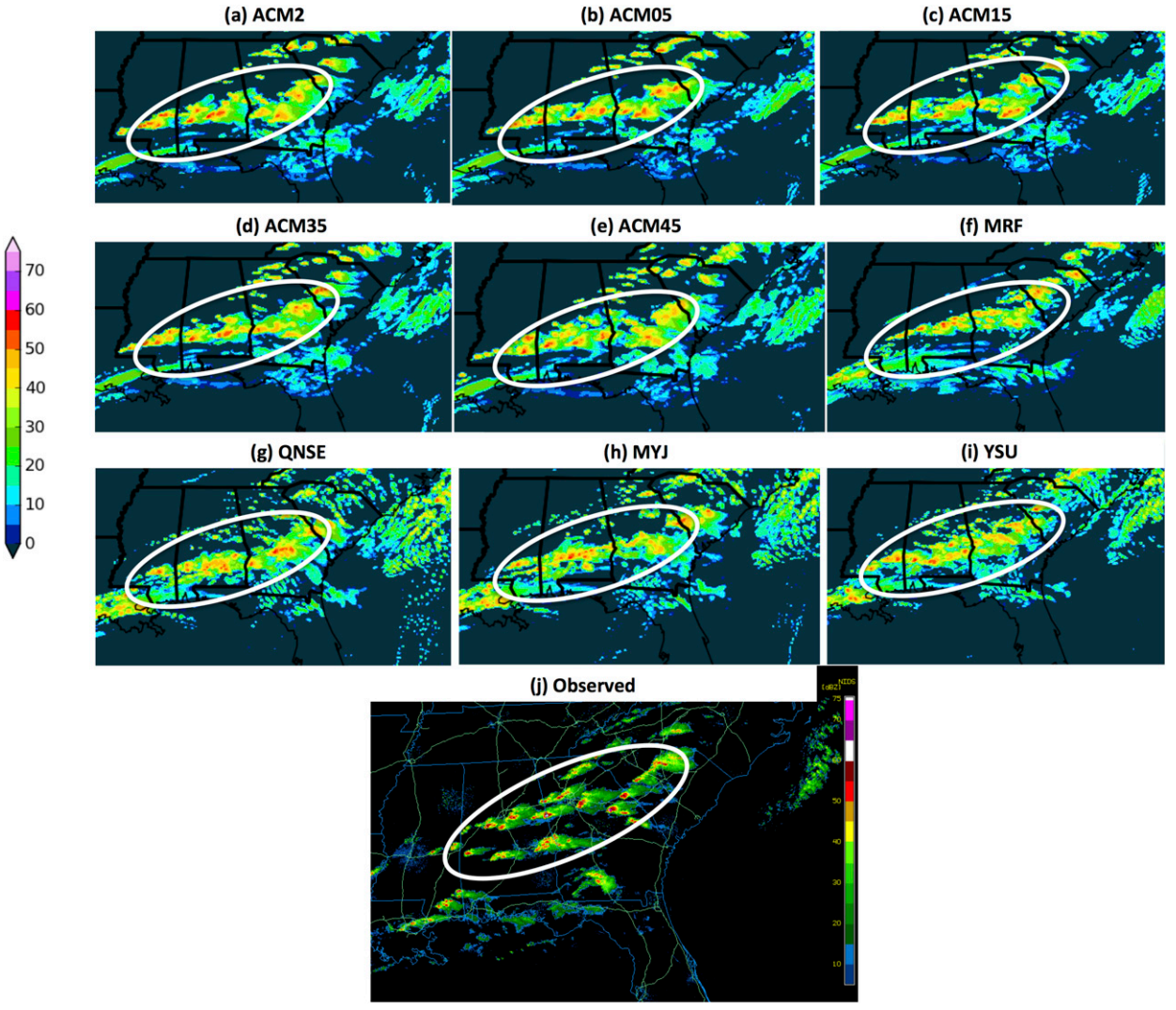

FIG. 21. As in Fig. 20, but for (a)–(i) the 13-h forecast valid at 0100 UTC 19 Feb 2009 and (j) the observed at 0057 UTC 19 Feb 2009 (closest archived time).

This entire set of model evaluations for already-developed PBL parameterization schemes, and modified ones, represents a new area of study through their application in an atmospheric regime not commonly studied. It is clear that the simultaneous representation of both nonlocal and local mixing is most appropriate for the SECOLD regime. The ACM2 (nonlocal–local) scheme and its variants most consistently reduce extreme forms of bias that making a selection of strictly local or nonlocal PBL parameterization schemes would produce. Among the variants of the ACM2 scheme, the ACM05 appears to produce PBL depth and 0–3-km lapse rate distributions most similar to RUC/SFCOA output, although by only a small margin compared to other variants. As such, this study has extended the current understanding of PBL-scheme performance forward into the SECOLD regime whose strong-shear and weak-instability characteristics are thoroughly documented by CCCB15 and references therein, effectively adding to previous research involving the evaluation of PBL parameterization scheme performance in a variety of regimes (e.g., Jankov et al. 2005; Hu et al. 2010; Nielsen-Gammon et al. 2010; Coniglio et al. 2013).

These findings can contribute substantially to guiding the numerical modeling and operational meteorology community to the most appropriate PBL parameterization scheme to be used in convection-allowing model guidance in the SECOLD regime. When considered in conjunction with analyses of rapidly evolving synoptic-scale and mesoscale mass fields governing forcing for ascent, a more complete understanding of the SECOLD regime can be achieved. Cursory attempts have been

performed to investigate the sensitivity of simulated composite reflectivity to altering the PBL scheme, and also to investigate biases in the RUC/SFCOA dataset in the SECOLD regime. Future research could, in further detail, investigate these phenomena. Furthermore, the effects of changing domain characteristics such as horizontal grid length, number of vertical levels, and other parameterization schemes such as microphysics could be foci for additional investigation for improving numerical models in this regime. Ultimately, this work sheds light on a severe weather forecast problem that has had relatively limited treatment in numerical modeling studies. The unique aspects of the SECOLD environment and many focused clues to assist with its depiction in numerical modeling identified throughout this work can give rise to additional investigation of this regime in future studies.

Acknowledgments. This work originates from the lead author's dissertation that he prepared for his Ph.D. at the University of Oklahoma School of Meteorology. He is indebted to his Ph.D. committee members—including Dr. Steven Cavallo, Dr. Harold Brooks, Dr. Frederick Carr, Dr. Kevin Kloesel, and Dr. John Greene—for all of their support. The authors greatly thank Richard Thompson, Bryan Smith, and Andrew Dean of the SPC for providing some of the data used in this study. Furthermore, the authors want to extend appreciation to Richard Thompson (SPC) for numerous discussions regarding this research and its implications, and numerous other SPC meteorologists for their helpful input, along with anonymous reviewers for their feedback. Steven Weiss (SPC) and Alan Gerard (National Severe Storms Laboratory) provided much guidance for this research. The lead author's father, Mr. Joel Cohen (a retired economist), provided substantial inspiration for the forecast evaluation methodologies performed in this manuscript. Finally, the authors are deeply appreciative of all of the guidance that Philip Schumacher (National Weather Service Sioux Falls, SD) provided as editor of this work. Philip's input undoubtedly improved this manuscript, and his dedication and patience as *Weather and Forecasting* editor were absolutely critical to the success of this work. The scientific results and conclusions, as well as any views or opinions expressed herein, are those of the authors and do not necessarily reflect the views of NOAA or the Department of Commerce.

REFERENCES

Ashley, W. S., 2007: Spatial and temporal analysis of tornado fatalities in the United States: 1880–2005. *Wea. Forecasting*, **22**, 1214–1228, doi:10.1175/2007WAF2007004.1.

Benjamin, S. G., and Coauthors, 2004: An hourly assimilation–forecast cycle: The RUC. *Mon. Wea. Rev.*, **132**, 495–518, doi:10.1175/1520-0493(2004)132<0495:AHACTR>2.0.CO;2.

Bothwell, P. D., J. A. Hart, and R. L. Thompson, 2002: An integrated three-dimensional objective analysis scheme in use at the Storm Prediction Center. *21st Conf. on Severe Local Storms/19th Conf. on Weather Analysis and Forecasting/15th Conf. on Numerical Weather Prediction*, San Antonio, TX, Amer. Meteor. Soc., JP3.1, https://ams.confex.com/ams/pdfpapers/47482.pdf.

Brooks, H. E., 2009: Proximity soundings for Europe and the United States from reanalysis data. *Atmos. Res.*, **93**, 546–553, doi:10.1016/j.atmosres.2008.10.005.

Burk, S. D., and W. T. Thompson, 1989: A vertically nested regional numerical weather prediction model with second-order closure physics. *Mon. Wea. Rev.*, **117**, 2305–2324, doi:10.1175/1520-0493(1989)117<2305:AVNRNW>2.0.CO;2.

Clements, K. W., and J. A. Frenkel, 1980: Exchange rates, money and relative prices: The dollar–pound in the 1920s. *J. Int. Econ.*, **10**, 249–262, doi:10.1016/0022-1996(80)90057-4.

Cohen, A. E., S. M. Cavallo, M. C. Coniglio, and H. E. Brooks, 2015: A review of planetary boundary layer parameterization schemes and their sensitivity in simulating southeastern U.S. cold season severe weather environments. *Wea. Forecasting*, **30**, 591–612, doi:10.1175/WAF-D-14-00105.1.

Coniglio, M. C., 2012: Verification of RUC 0–1-h forecasts and SPC mesoscale analyses using VORTEX2 soundings. *Wea. Forecasting*, **27**, 667–683, doi:10.1175/WAF-D-11-00096.1.

——, J. Correia, P. T. Marsh, and F. Kong, 2013: Verification of convection-allowing WRF model forecasts of the planetary boundary layer using sounding observations. *Wea. Forecasting*, **28**, 842–862, doi:10.1175/WAF-D-12-00103.1.

Edwards, R., A. R. Dean, R. L. Thompson, and B. T. Smith, 2012: Convective modes for significant severe thunderstorms in the contiguous United States. Part III: Tropical cyclone tornadoes. *Wea. Forecasting*, **27**, 1507–1519, doi:10.1175/WAF-D-11-00117.1.

Ek, M. B., K. E. Mitchell, Y. Lin, P. Grunmann, E. Rodgers, G. Gayno, and V. Koren, 2003: Implementation of the upgraded Noah land surface model in the NCEP operational mesoscale Eta model. *J. Geophys. Res.*, **108**, 8851, doi:10.1029/2002JD003296.

Güldner, J., and D. Spänkuch, 2001: Remote sensing of the thermodynamic state of the atmospheric boundary layer by ground-based microwave radiometry. *J. Atmos. Oceanic Technol.*, **18**, 925–933, doi:10.1175/1520-0426(2001)018<0925:RSOTTS>2.0.CO;2.

Guyer, J. L., and A. R. Dean, 2010: Tornadoes within weak CAPE environments across the continental United States. *25th Conf. on Severe Local Storms*, Denver, CO, Amer. Meteor. Soc., 1.5, https://ams.confex.com/ams/25SLS/techprogram/paper_175725.htm.

——, D. A. Imy, A. Kis, and K. Venable, 2006: Cool season significant (F2–F5) tornadoes in the Gulf Coast states. *23rd Conf. on Severe Local Storms*, St. Louis, MO, Amer. Meteor. Soc., 4.2, https://ams.confex.com/ams/23SLS/techprogram/paper_115320.htm.

Hacker, J. P., 2010: Spatial and temporal scales of boundary layer wind predictability in response to small-amplitude land surface uncertainty. *J. Atmos. Sci.*, **67**, 217–233, doi:10.1175/2009JAS3162.1.

Holton, J. R., 2004: *Introduction to Dynamic Meteorology*. 4th ed. Elsevier, 535 pp.

Holtslag, A. A. M., E. I. F. De Bruijn, and H.-L. Pan, 1990: A high resolution air mass transformation model for short-range weather forecasting. *Mon. Wea. Rev.*, **118**, 1561–1575, doi:10.1175/1520-0493(1990)118<1561:AHRAMT>2.0.CO;2.

Hong, S.-Y., and H.-L. Pan, 1996: Nonlocal boundary layer vertical diffusion in a medium-range forecast model. *Mon. Wea.*

Rev., **124**, 2322–2339, doi:10.1175/1520-0493(1996)124<2322:NBLVDI>2.0.CO;2.

——, and J. O. J. Lim, 2006: The WRF single-moment 6-class microphysics scheme (WSM6). *J. Korean Meteor. Soc.*, **42**, 129–151.

——, Y. Noh, and J. Dudhia, 2006: A new vertical diffusion package with an explicit treatment of entrainment processes. *Mon. Wea. Rev.*, **134**, 2318–2341, doi:10.1175/MWR3199.1.

Hu, X.-M., J. W. Nielsen-Gammon, and F. Zhang, 2010: Evaluation of three planetary boundary layer schemes in the WRF model. *J. Appl. Meteor. Climatol.*, **49**, 1831–1844, doi:10.1175/2010JAMC2432.1.

Iacono, M. J., J. S. Delamere, E. J. Mlawer, M. W. Shephard, S. A. Clough, and W. D. Collins, 2008: Radiative forcing by long-lived greenhouse gases: Calculations with the AER radiative transfer models. *J. Geophys. Res.*, **113**, D13103, doi:10.1029/2008JD009944.

Janjić, Z. I., 1990: The step-mountain coordinate: Physical package. *Mon. Wea. Rev.*, **118**, 1429–1443, doi:10.1175/1520-0493(1990)118<1429:TSMCPP>2.0.CO;2.

——, 1994: The step-mountain eta coordinate model: Further developments of the convection, viscous sublayer, and turbulence closure schemes. *Mon. Wea. Rev.*, **122**, 927–945, doi:10.1175/1520-0493(1994)122<0927:TSMECM>2.0.CO;2.

Jankov, I., W. A. Gallus Jr., M. Segal, B. Shaw, and S. E. Koch, 2005: The impact of different WRF model physical parameterizations and their interactions on warm season MCS rainfall. *Wea. Forecasting*, **20**, 1048–1060, doi:10.1175/WAF888.1.

Kain, J. S., M. E. Baldwin, P. R. Janish, S. J. Weiss, M. P. Kay, and G. W. Carbin, 2003: Subjective verification of numerical models as a component of a broader interaction between research and operations. *Wea. Forecasting*, **18**, 847–860, doi:10.1175/1520-0434(2003)018<0847:SVONMA>2.0.CO;2.

——, S. J. Weiss, M. E. Baldwin, G. W. Carbin, D. A. Bright, J. J. Levit, and J. A. Hart, 2005: Evaluating high-resolution configurations of the WRF Model that are used to forecast severe convective weather: The 2005 SPC/NSSL Spring Program. *21st Conf. on Weather Analysis and Forecasting/17th Conf. on Numerical Weather Prediction*, Washington, DC, Amer. Meteor. Soc., 2A.5, https://ams.confex.com/ams/WAFNWP34BC/techprogram/paper_94843.htm.

——, and Coauthors, 2013: A feasibility study for probabilistic convection initiation forecasts based on explicit numerical guidance. *Bull. Amer. Meteor. Soc.*, **94**, 1213–1225, doi:10.1175/BAMS-D-11-00264.1.

King, J. R., M. D. Parker, K. D. Sherburn, and G. M. Lackmann, 2017: Rapid evolution of cool season, low-CAPE severe thunderstorm environments. *Wea. Forecasting*, **32**, 763–779, doi:10.1175/WAF-D-16-0141.1.

Kis, A. K., and J. M. Straka, 2010: Nocturnal tornado climatology. *Wea. Forecasting*, **25**, 545–561, doi:10.1175/2009WAF2222294.1.

Massey, F. J., 1951: The Kolmogorov–Smirnov test for goodness of fit. *J. Amer. Stat. Assoc.*, **46**, 68–77, doi:10.1080/01621459.1951.10500769.

NCAR, 2017: Image archive: Meteorological case study selection kit. National Center for Atmospheric Research/Mesoscale and Microscale Meteorology Laboratory, http://www2.mmm.ucar.edu/imagearchive/.

Nielsen-Gammon, J. W., X.-M. Hu, F. Zhang, and J. E. Pleim, 2010: Evaluation of planetary boundary layer scheme sensitivities for the purpose of parameter estimation. *Mon. Wea. Rev.*, **138**, 3400–3417, doi:10.1175/2010MWR3292.1.

NOAA/NCDC, 2014a: Model data. NOAA/National Operational Model Archive and Distribution System, http://nomads.ncdc.noaa.gov/data.php?name5inventory.

——, 2014b: RUC online archive. NOAA/National Operational Model Archive and Distribution System, http://nomads.ncdc.noaa.gov/data/ruc/.

NOAA/NCEP, 2000: NCEP FNL Operational Model Global Tropospheric Analyses, continuing from July 1999 (updated daily). NCAR Computational and Information Systems Laboratory Research Data Archive, accessed 31 December 2015, https://doi.org/10.5065/D6M043C6.

Pindyck, R. S., and D. L. Rubinfeld, 1981: *Econometric Models and Economic Forecasts*. 2nd ed. McGraw-Hill, 630 pp.

Pleim, J. E., 2007a: A combined local and nonlocal closure model for the atmospheric boundary layer. Part I: Model description and testing. *J. Appl. Meteor. Climatol.*, **46**, 1383–1395, doi:10.1175/JAM2539.1.

——, 2007b: A combined local and nonlocal closure model for the atmospheric boundary layer. Part II: Application and evaluation in a mesoscale meteorological model. *J. Appl. Meteor. Climatol.*, **46**, 1396–1409, doi:10.1175/JAM2534.1.

Schaefer, J. T., 1986: Severe thunderstorm forecasting: A historical perspective. *Wea. Forecasting*, **1**, 164–189, doi:10.1175/1520-0434(1986)001<0164:STFAHP>2.0.CO;2.

Sherburn, K. D., and M. D. Parker, 2014: Climatology and ingredients of significant severe convection in high-shear, low-CAPE environments. *Wea. Forecasting*, **29**, 854–877, doi:10.1175/WAF-D-13-00041.1.

Skamarock, W. C., and Coauthors, 2008: A description of the Advanced Research WRF version 3. NCAR Tech. Note NCAR/TN-475+STR, 113 pp., http://dx.doi.org/10.5065/D68S4MVH.

Smith, B. T., R. L. Thompson, J. S. Grams, C. Broyles, and H. E. Brooks, 2012: Convective modes for significant severe thunderstorms in the contiguous United States. Part I: Storm classification and climatology. *Wea. Forecasting*, **27**, 1114–1135, doi:10.1175/WAF-D-11-00115.1.

Stensrud, D. J., 2007: *Parameterization Schemes: Keys to Understanding Numerical Weather Prediction Models*. Cambridge University Press, 459 pp.

Storm Prediction Center, 2015: SPC National Severe Weather database browser: Online SeverePlot 3.0. NOAA/NWS/Storm Prediction Center, http://www.spc.noaa.gov/climo/online/sp3/plot.php.

Stull, R. B., 1988: *An Introduction to Boundary Layer Meteorology*. Kluwer Academic, 666 pp.

Sukoriansky, S., B. Galperin, and V. Perov, 2005: Application of a new spectral theory of stably stratified turbulence to the atmospheric boundary layer over sea ice. *Bound.-Layer Meteor.*, **117**, 231–257, doi:10.1007/s10546-004-6848-4.

Theil, H., 1961: *Economic Forecasts and Policy*. 2nd ed. North-Holland, 567 pp.

——, 1966: *Applied Economic Forecasting*. North-Holland, 474 pp.

Thompson, R. L., B. T. Smith, J. S. Grams, A. R. Dean, and C. Broyles, 2012: Convective modes for significant severe thunderstorms in the contiguous United States. Part II: Supercell and QLCS tornado environments. *Wea. Forecasting*, **27**, 1136–1154, doi:10.1175/WAF-D-11-00116.1.

Trapp, R. J., S. A. Tessendorf, E. S. Godfrey, and H. E. Brooks, 2005: Tornadoes from squall lines and bow echoes. Part I: Climatological distribution. *Wea. Forecasting*, **20**, 23–34, doi:10.1175/WAF-835.1.

Trnka, M., J. Eitzinger, G. Gruszczynski, K. Buchgraber, R. Resch, and A. Schaumberger, 2006: A simple statistical model for predicting herbage production from permanent grassland. *Grass Forage Sci.*, **61**, 253–271, doi:10.1111/j.1365-2494.2006.00530.x.